

Fast and Effective Catalytic Degradation of an Organic Dye by Eco-friendly Capped ZnS and Mn doped ZnS nanocrystals

Sabri Ouni

Universite de Kairouan

Naim Bel Haj Mohamed (✉ naimhajmed@gmail.com)

Universite de Kairouan <https://orcid.org/0000-0003-2952-4265>

Noureddine Chaaben

University of Monastir: Universite de Monastir

Adrian Bonilla-Petriciolet

Aguascalientes Institute of Technology: Instituto Tecnologico de Aguascalientes

Mohamed Haouari

University of Monastir: Universite de Monastir

Research Article

Keywords: ZnS-TGA, eco-friendly nanocrystals, Azo dye, photodegradation, Wastewaters

Posted Date: November 15th, 2021

DOI: <https://doi.org/10.21203/rs.3.rs-766624/v1>

License: © ⓘ This work is licensed under a Creative Commons Attribution 4.0 International License.

[Read Full License](#)

Version of Record: A version of this preprint was published at Environmental Science and Pollution Research on January 14th, 2022. See the published version at <https://doi.org/10.1007/s11356-021-17860-1>.

1 **Fast and effective catalytic degradation of an organic dye by eco-friendly capped ZnS**
2 **and Mn doped ZnS nanocrystals**

3
4 Sabri Ouni^a, Naim Bel Haj Mohamed^b, Nouredine Chaaben^c, Adrián Bonilla-Petriciolet^d,
5 Mohamed Haouari^a

6 ^a*Laboratory of Advanced Materials and Interfaces (LIMA), Faculty of Sciences of Monastir, University*
7 *of Monastir, Avenue of the environment, 5019 Monastir, Tunisia*

8 ^b*Laboratory of Spectroscopic Characterization and Optical Materials (LaSCOM), University of Sfax,*
9 *Faculty of Sciences B.P. 1171, 3000, Sfax-Tunisia*

10 ^c*Research unit on hetero-Epitaxies and Applications ; Faculty of Sciences of Monastir, University of*
11 *Monastir, Avenue of the environment, 5019 Monastir, Tunisia*

12 ^d*Instituto Tecnológico de Aguascalientes, Aguascalientes, 20256, México*

13 **Corresponding authors: E-mail: naimhajmed@gmail.com; Sabriouni1995@gmail.com*

14
15
16
17
18
19
20
21
22
23
24
25
26
27
28
29
30
31
32
33
34
35
36
37
38
39
40
41
42
43
44
45

46 **Abstract:**

47 Undoped and Mn-doped ZnS nanocrystals encapsulated with thioglycolic acid were
48 synthesized and characterized with different techniques, and finally tested in the
49 photodegradation of a methyl orange in aqueous solution under UV and sunlight irradiations.
50 FTIR and X-ray diffraction results confirmed the functionalization of these nanocrystals
51 surface by thioglycolic acid and the formation of crystalline structures of ZnS and Mn-doped
52 ZnS with cubic and hexagonal phases. Calculated average size of ZnS nanocrystals was in the
53 range of 2 - 3 nm. It was observed a blue shift of the absorbance threshold and the estimated
54 bandgap energies were higher than that of Bulk ZnS thus confirming the quantum
55 confinement effect of charge carriers. Photoluminescence spectra of ZnS nanocrystals
56 exhibited emission in the range of 410- 490 nm and the appearance of an additional emission
57 band around 580 nm (2.13eV) connected to the $^4T_1 \rightarrow ^6A_1$ transition of the Mn^{2+} ions.
58 Photodegradation of methylene orange with undoped and Mn-doped ZnS-TGA nanocrystals
59 was investigated. Dye adsorption prior to photocatalysis using nanocrystals was studied via
60 kinetic experiments and statistical physics models. The maximum dye adsorption capacity on
61 doped ZnS-TGA was ~ 26.98 mg/g. The adsorption kinetic was found to follow the pseudo-
62 second-order kinetic model. According to the statistical physics results, the calculated
63 adsorption energy was 22.47-23.47 kJ/mol and it showed that the dye adsorption was
64 associated to the hydrogen interaction where the removal process was feasible and multi-
65 molecular. The photocatalytic activity of undoped ZnS nanoparticles under UV irradiation
66 showed better efficiency than doped nanocrystals thus indicating that manganese doping
67 generated a dropping of the photocatalytic degradation of the dye. Dye degradation efficiency
68 of 81.37% using ZnS-TGA nanocrystals was achieved after 6 min, which indicated that
69 ZnMnS-TGA nanocrystals may be considered as an alternative low cost and environmental
70 friendly material for facing water pollution caused by organic compounds via
71 photodegradation processes.

72 **Keywords:** ZnS-TGA; eco-friendly nanocrystals; Azo dye; photodegradation, Wastewaters

73 **1. Introduction:**

74 Semiconductors nanoparticles (NPs) have found numerous applications in different
75 technological fields going from photovoltaic devices to medical imaging, lasers, LEDs and
76 photocatalysis (Dao 2020; Rtimi et al. 2021; Meikle et al. 2020; Long et al. 2020; Su et al.
77 2020; Li et al. 2019; Daskalakis et al. 2020; Rtimi et al. 2021). These applications are
78 supported by their unique properties as compared to their bulk counterpart, which arise from

79 the confinement of the charge carriers as a result of their small sizes. This quantum
80 confinement effect enlarges the energy bandgap, which makes the electronic and optical
81 properties size dependent allowing the control of the absorption and the emission wavelengths
82 of these materials. Additionally, semiconductor NPs have a large surface to volume ratio,
83 which is responsible for a significant change in their physical and chemical properties. Indeed,
84 the surface atoms are less coordinated than internal ones. This makes these NPs lesser stable
85 against aggregation and more reactive with their environment in comparison to bulk materials.
86 Additionally, the dangling bonds and surface defects introduce energy levels in the bandgap,
87 which are usually responsible for non-radiative transitions and the emission quenching of
88 semiconductor NPs. To prevent the agglomeration and the drawbacks of surface defects, NPs
89 must be grown within a protecting medium such as glass and polymer or enrobed by
90 encapsulating molecules that should be well fixed at their surface.

91 Recently, semiconductor NPs have emerged as promising photocatalysts to produce hydrogen
92 by water dissociation or to degrade organic pollutants in wastewater being more effective than
93 the conventional methods (Buthiyappan et al. 2016). However, these NPs must be dispersible
94 in water to maximize their performance. Accordingly, the colloidal wet chemical synthesis
95 has emerged as the most popular safe way to produce, at large scale and cost-effective, water-
96 soluble semiconductor NPs with narrow size dispersion and promising optical and electronic
97 properties (Jaldurgam et al. 2021).

98 Among the different semiconducting nanostructures, ZnS NPs are recognized as
99 environmentally friendly and effective photocatalyst for the degradation of organic pollutants
100 in wastewaters. This is due to their nontoxicity when they are used in small amounts and their
101 unique electronic and optical properties. Moreover, ZnS NPs have a high absorption
102 coefficient required for solar light harvesting, which is the first step for the photodegradation
103 of organic pollutants at industrial level. They have also a high negative reduction-oxidation
104 potential of excited electrons due to their higher conduction band position in an aqueous
105 solution as compared to other extensively studied photocatalysts (Yang et al. 2014).
106 Additionally, these NPs are able to rapidly generate great density of electron-hole pairs under
107 photoexcitation because of their direct bandgap (Arao et al. 2009), and they show competitive
108 photocatalytic activity due to trapped holes arising from surface defects (Saenger et al. 1998).
109 The photocatalytic activity of these semiconductor NPs is due to the formation of OH^* and O_2^-
110 free radicals that results from the reaction of the photo-generated holes and electrons with
111 water and free oxygen molecules, respectively. However, ZnS nanocrystals (NCs) that belong

112 to large bandgap semiconductors (3.7 eV) can absorb only UV radiation, which reduces their
113 photoactivity. One way to enhance the efficiency of these nanostructures and to improve their
114 visible light harvesting efficiency is to extend the wavelength range photoactivity towards
115 visible light region of solar spectrum by doping them by transition metal ions such as Mn^{2+} ,
116 Ni^{2+} , Cu^{2+} (Kostrov et al. 2020; Kabachii et al. 2021; Wang et al. 2017; Chauhan et al. 2014;
117 Othman et al. 2020). The doping impurities introduce trapping levels in the bandgap that
118 reduces the carrier's recombination probability and allows them to diffuse faster to the NCs
119 surface. With the aim to obtain an efficient, low- cost and eco-friendly nanocatalysts that can
120 be used at industrial scale, this paper reports the synthesis and application of ZnS and Mn-
121 doped ZnS NPs via colloid method. The physico-chemical properties of these nanostructures
122 were investigated and their photocatalytic activity to decompose methylene orange (MO) dye
123 was evaluated by conducting degradation experiments under UV and sunlight.

124 **2. Methodology**

125 **2.1. Chemicals**

126 All chemicals were purchased from Sigma-Aldrich. They were of analytical grade and used
127 without any purification process. They included zinc (II) acetate dihydrate (Sigma-Aldrich,
128 $Zn[CH_3COO]_2 \cdot 2H_2O \geq 98\%$), manganese sulfate ($MnSO_4$), sodium sulfide (Sigma-Aldrich,
129 $Na_2S \geq 98\%$), thioglycolic acid (TGA) (Sigma-Aldrich, $HSCH_2COOH$, 97%), sodium
130 hydroxide (NaOH, 99%) and methylene orange dye (Sigma-Aldrich, $C_{14}H_{14}N_3NaO_3S \geq 50\%$,
131 $MW = 327.33$ g/mol). All aqueous solutions were prepared with ultra-pure water.

132 **2.2. Synthesis of TGA capped ZnS nanoparticles**

133 Undoped ZnS and Mn-doped ZnS NCs were prepared using the colloidal hydrothermal
134 reaction method (Ouni et al. 2021), see *Figure 1*. The experimental synthesis protocol is
135 briefly described as follows. An aqueous solution was prepared by mixing dihydrated zinc
136 acetate (2 mmol) with TGA (5 mmol) in 100 mL of water. Manganese sulphate was added at
137 different percentages in weight (4, 8 and 12%) with respect to zinc for each synthesis. The pH
138 of the resulting mixture was adjusted to 11 by drop addition of NaOH (1 M) with continuous
139 agitation under N_2 for 30 min. The second step of this synthesis protocol was based on the
140 injection of S^{2-} (0.08 mmol) at room temperature into the solution containing Zn^{2+} -TGA
141 complexes. The mixture was then heated at 100°C for 3h. Finally, the reaction mixture was
142 cooled to room temperature to stop the NCs growth. After solution cooling and drying,

143 undoped and Mn-doped ZnS NCs were purified by precipitation with ethanol, washed two
144 times with ethanol and stored in vacuum at room temperature.

145 **2.3. NCs characterization**

146 X-ray diffraction (XRD) characterization was performed using Philips X'Pert PRO MPD
147 diffractometer equipped with a Cu K α source of wavelength $\lambda = 1,542\text{\AA}$. Transmission
148 electron microscopy (TEM) images were obtained using a FEI Tecnai G2 electron microscope
149 operated at an accelerating voltage of 200 kV and equipped with Energy Dispersive X-ray
150 (EDX) for element chemical analysis. Samples were analyzed by placing a drop of aqueous
151 suspension of particles onto a carbon film on a copper grid. Fourier transform infrared (FTIR)
152 spectra were recorded at room temperature with a Perkin Elmer version 5.3 within the
153 wavenumber range of 400-4000 cm^{-1} and using KBr pellets. UV-visible absorption spectra
154 were obtained at room temperature in the range of 200-800 nm using a SPECORD 210 Plus
155 spectrophotometer with quartz cuvettes. Photoluminescence (PL) spectra were recorded at
156 room temperature using conventional photoluminescence setup and a helium cadmium laser
157 as excitation source ($\lambda_{exc}=325\text{nm}$).

158 **2.4. Dye adsorption experiments: kinetics and isotherms**

159 Dye adsorption experiments were performed at 300 K in a batch system. In a typical
160 experiment, 50 mL of dye solution with different initial concentrations and 50 mg of nano-
161 catalyst (m) were used for these studies. The adsorption experiments were carried out at pH 7.
162 Adsorption parameters like time contact and dye concentration were investigated. Kinetic
163 studies were performed with MO dye concentrations from 10 to 50 mg/L with a sampling
164 period of 120 min and magnetic stirring in the dark to measure the MO adsorption capacities.
165 The concentration of dye solution was determined using SPECORD 210 Plus UV-Vis
166 spectrometer at 465 nm. MO dye adsorption capacities Q_e (mg/g) were calculated using the
167 next equation

$$168 \quad Q_e = \frac{V(C_0 - C_e)}{m} \quad (1)$$

169 where C_0 is the initial dye concentration (mg/L), C_e is the equilibrium dye concentration in
170 the solution (mg/L), V is the dye solution volume (mL) and W is the weight of the nano-
171 adsorbent (mg).

172

173

174

175

176 **2.5. Photocatalytic degradation tests**

177 The photocatalytic efficiency of the undoped and Mn-doped ZnS NCs was evaluated via the
178 photodegradation of MO dye as a model molecule of an organic pollutant. Before starting the
179 photocatalytic degradation experiments, the aqueous solutions containing both dye and NCs
180 were submitted to a vigorous magnetic stirring in dark for 2 h in order to ensure the
181 adsorption/desorption equilibrium (Chan et al. 2011). Then, they were submitted to irradiation
182 by mercury lamp of 160W to monitor the MO degradation. Solution samples were taken at
183 regular time intervals and analyzed by UV-visible spectroscopy to determine the absorbance
184 at 465 nm, which corresponded to the maximum absorption of MO molecule. Degradation
185 experiments were also conducted under sunlight.

186 **3. Results and discussion**

187 **3.1. Structural and morphological characterization of NCs**

188 FTIR spectra of the different samples are shown in *Figure 2*. All these spectra showed an
189 absorption band at 563 cm^{-1} that was attributed to the stretching vibrations of Zn-
190 S (Amaranatha Reddy et al. 2014). The spectra of ZnS NCs doped with different
191 concentrations of Mn^{2+} showed the presence of the same absorption bands at wavenumber
192 values close to those recorded with pure ZnS and no other apparent bands to other vibration
193 modes of doping impurities or other elements were observed. These spectra also showed a
194 wide band at $\sim 3360\text{ cm}^{-1}$, which was associated to the elongation vibration of (O-H) groups
195 of TGA ligand (Liu et al. 2008). FTIR spectrum of TGA showed the presence of a
196 characteristic band at 2560 cm^{-1} related to the S-H bond (Dehghan et al. 2018). This
197 absorption band was absent in TGA-capped ZnS NCs spectra thus indicating the rupture of S-
198 H bond and the fixation of the sulfur atom on the NCs surface (Xie et al. 2011). This finding
199 can be explained by the strong interaction of the sulfur electron pair with zinc atoms on the
200 surface (Ouni et al. 2021). In addition, these spectra contained absorption bands around 570-
201 700, 850, 1429, 1508 and 1627 cm^{-1} assigned to (C-S), (C-H), (COO^-), (C=O) and (-OH)
202 bonds, respectively (Amirian et al. 2018). These results clearly demonstrated that NCs were
203 well functionalized by TGA ligand, which allowed the control of their growth during
204 synthesis and prevented NCs aggregation (Singh and Chauhan 2009).

205 *Figure 3* shows the XRD pattern of the undoped and Mn-doped ZnS samples. In the case of
206 undoped ZnS NCs, XRD diffraction patterns contained peaks at $2\theta = 28.95, 33.76, 47.58$ and
207 55.27° . These peaks were attributed to the diffraction plans (111), (200), (220) and (311) of

208 the zinc blende phase (ZB) of ZnS according to JCPDS (80-0007). However, it was also
209 observed the existence of a diffraction peak at $2\theta = 31.08^\circ$ that corresponded to the (101) plan
210 of the wurtzite phase (WZ) of ZnS (JCPDS 80-0020). This structural anomaly made the
211 distinction between the cubic and hexagonal structures very difficult. The most intense peak
212 attributed to (111) suggested that NCs growth in this direction was preferred and confirmed
213 that the structure of ZnS NCs was almost cubic. XRD patterns were adjusted with Gaussian
214 profiles to calculate the full-width-at-half-maximum (FWHM) of identified peaks and these
215 values were used to estimate the crystallite size according to Scherrer formula (Jothibas et al.
216 2018):

$$217 \quad D = \frac{K\lambda}{\beta \cos(\theta)} \quad (2)$$

218 Where D is the average crystallite size (nm), λ is the wavelength of X-ray (1.5402Å) Cu $K\alpha$
219 radiation, K is the shape factor (0.9), β is the measured full width at half maximum of the
220 diffraction peak and θ is the Bragg diffraction angle. The average size of the undoped ZnS
221 NCs was estimated to be ~ 7.15 nm, while the lattice parameter was 5.38 Å.

222 For Mn-doped NCs, the peaks at 29.52° , 31.82° , 47.31° and 56.12° were assigned to the
223 plans (002), (101), (110) and (200) of the hexagonal structure according to the JCPDS
224 hexagonal ZnS standard sheet (80-0007). However, the presence of the peak associated with
225 the crystallographic plane (200) was around 34.77° thus indicating the presence of the cubic
226 phase of ZnS. Similar results were reported for ZnS NCs synthesized by precipitation in an
227 aqueous medium (Chauhan et al. 2014). The estimated crystallite sizes are given in **Table 1**.
228 NCs size decreased from 7.15 to 2.5 nm with the increment of Mn doping content up to 12%.
229 This result indicated that Zn^{2+} ions were replaced by Mn^{2+} ions in the ZnS matrix. The
230 reduction of ZnS NCs size with the doping concentration could be explained by the induced
231 NCs growth and enhancement of surface area to volume ratio in the system (Mote et al.
232 2013). This result confirmed the incorporation of manganese into the host lattice of ZnS and
233 the formation of Mn-doped ZnS NCs. However, the Scherrer formula takes into account only
234 the broadening effect of the spectra coming from the different diffracting domains and does
235 not include the intrinsic micro-strain effect created within the lattice by stacking fault, point
236 defect and grain boundary (Poornaprakash et al. 2018; Pandya et al. 2016). Therefore, the
237 change of NCs size may be correlated to different structural parameters including the lattice
238 strain (ϵ), dislocation density (δ) and stacking fault (SF). These parameters can be estimated
239 by using the next formula (Nath et al. 2020; Jothibas et al. 2016; Bel Haj Mohamed et al.
240 2021) and the calculated values are summarized in **Table 1**.

$$\varepsilon = \frac{\beta \cos(\theta)}{4} \quad (3)$$

$$\delta = \frac{1}{D^2} \quad (4)$$

$$SF = \frac{2\pi^2}{45(\tan\theta)^2} \beta_{hkl} \quad (5)$$

244 The value of dislocation density can be associated to the amount of defects and vacancies in
 245 the crystals. Results showed that δ increased with the doping Mn content from zero to 12%.
 246 This was due to the inversely proportional relationship between the dislocation and the size of
 247 NCs. Thus, the smallest particles (ZnS: Mn 12%) have the highest possibility of dislocations
 248 since they have a tendency to minimize their higher surface energy (Gaceur et al. 2012).
 249 Undoped ZnS NCs with the highest size were the most ordered compared to Mn-doped ZnS.
 250 This finding made obvious the effect of doping with Mn on the change of the high orientation
 251 plane from (111) to (101) as well as the improvement of crystallinity. Both micro-strain and
 252 stacking fault showed the same trends when they decreased with increasing the doping ratio
 253 except for the case of Mn 8%. The decreasing of micro-strain indicated that the Mn-doped
 254 ZnS samples contained lattice defects and vacancies. On the other hand, SF describes the
 255 disordering of crystallographic planes. Therefore, the decreasing tendency of SF suggested
 256 that the defects increased by substituting zinc by manganese.

257 **Figure 4** shows TEM images of tested samples and the corresponding size distribution
 258 histograms. NCs exhibited a spherical shape and were agglomerated probably due to the
 259 insufficient ligand amount to cover all ZnS NCs and inhibited the aggregation and formation
 260 of large clusters. This agglomeration may be also due to high particles concentrations used in
 261 TEM experiments. From the histograms of undoped and Mn (8%)-doped NCs, it was found
 262 that the average NCs diameters were 5.9 and 4.1 nm (± 0.5 nm), respectively. These results
 263 demonstrated that Mn-doping decreased the ZnS particle size. The inter-planar distance were
 264 determined from digital micrograph for undoped and doped ZnS and it was 0.36 nm, which
 265 corresponded to the plane (111) of the ZB phase and 0.2 nm for the plane (101) of the WZ
 266 phase, respectively. These results are consistent with the values found by XRD measurements.
 267 EDX spectra for ZnS and Mn-doped ZnS NCs are shown in **Figure 5**. In particular, **Figure 5a**
 268 indicated the presence of Zn and S that were the major elemental components with also the
 269 presence of Si related to the detector signal. It was observed the presence of the carbon,
 270 oxygen and copper peaks that were related to TEM grid and ligand stabilizer. Results of Mn
 271 (8%)-doped NCs (**Figure 5b**) showed the presence of Zn, S and Mn, which confirmed the
 272 formation of doped NCs. This diagram also indicated the existence of carbon, oxygen and

273 silicon related to TGA ligand and TEM devices. Others peaks related to Al, Ca, K, Ni and Fe
274 were also detected probably due to residues coming from the main precursors during the
275 synthesis. Hence, TEM results indicated the formation of undoped and doped ZnS NCs that
276 were properly stabilized by TGA.

277 3.2.Optical characterization of NCs

278 UV-visible absorption spectra of the different NCs are reported in **Figure 6**. They showed a
279 blue shift of the absorption threshold when increasing Mn²⁺concentration. The absorption
280 threshold was 307, 300, 298 and 290 nm for 0, 4, 8 and 12% Mn-doping concentrations,
281 respectively. In accordance with the average sizes obtained from XRD analysis, this behavior
282 was explained by the presence of small Mn-doped ZnS NCs, which induced the widening of
283 gap energy(Meng et al. 1995).

284 The Tauc equation was utilized to estimate the gap energy of undoped and Mn-doped ZnS
285 NCs(Kaur et al. 2015).

$$286 \quad \alpha hv = A (hv - E_g)^n \quad (6)$$

287 where α is the absorption coefficient, A is a constant, hv is the photon energy, E_g is the
288 optical gap of NCs and n is a constant with $n = 1/2$ for direct semiconductors. The optical band
289 gap energy of NCs were estimated from the intercept of the extrapolation of Tauc plots with
290 the x-axis (**Figure 7**) and the results of the optical gap energies are displayed in **Table2**.

291 The calculated value of the optical gap energy of NCs increased from 3.75 to 3.92 eV with
292 increasing manganese doping. This variation in E_g was attributed to variations of NCs size by
293 the incorporation of manganese ions in the zinc substitute position within the ZnS structure.
294 At high doping concentrations, manganese ions caused a significant increment of E_g . This
295 finding was explained by the Burstein-Moss effect, which demonstrated that the excitation of
296 an electron from the valence band to conduction band in a doped semiconductor required
297 more energy due to the accumulation of electrons in the conduction band caused by the
298 shallow donor states (i.e., the movement of the Fermi level to the conduction band by doping
299 effect)(Brus 1986).

300 The average NPs sizes were also estimated by using the optical gap energy and the effective
301 mass approximation according to the next equation (Jai Kumar and Mahesh 2017; Mansur and
302 Mansur 2011):

$$303 \quad E_g^n = E_g^b + \frac{h^2}{8R^2} \left(\frac{1}{m_e^*} + \frac{1}{m_h^*} \right) - \frac{1.8e^2}{4\pi\epsilon R} \quad (7)$$

304 where E_g^n and E_g^b are the band gap energies of NPs and bulk material, respectively, m_e^* and m_h^*
305 are the effective masses of the electron and hole, e is the elementary electric charge and ϵ is

306 the dielectric constant of ZnS. It was observed a reduction in the size of the doped ZnS NCs
307 from 2.3 to 1.9 nm as the doping rate increased. The difference between the sizes found by
308 absorption spectroscopy and DRX was attributed to the fact that calculation of the latter values
309 were based on the effective mass approximation assuming that the NCs geometry was
310 spherical; while the XRD measurements in polydisperse systems were weighted to the largest
311 particles (Pejjai et al. 2017). Additionally, when the quantum dots are small enough, the
312 carrier's wave functions overlaps with the crystal boundaries thus resulting in energy
313 dependent effective masses (Jai Kumar and Mahesh 2017; Mansur and Mansur 2011). This
314 discrepancy may be also due to the fact that XRD results were obtained for powdered NCs,
315 while absorption measurement involved NCs dispersed in solution.

316 **Figure 8** shows the room-temperature photoluminescence spectra of undoped and Mn-doped
317 ZnS NCs with different Mn concentrations. PL spectra of pure ZnS nanocrystals showed two
318 wide and asymmetrical bands. Accordingly, they were convoluted with three Gaussian curves,
319 see **Figure 9**. The observed emission spectra may be the result of several emissions transition
320 essentially caused by the size distributions of the ZnS NCs with a large contribution of surface
321 defects. In fact, the stoichiometric ratio of synthetic precursor ($Zn/S \sim 2.5$) and the synthesis
322 method were responsible for the formation of punctual defects (interstitials, substitutes) or
323 extended (dislocations, aggregates, cavities) within the ZnS structure. Indeed, the use of
324 excess zinc caused that defects present in the ZnS NCs correspond to zinc interstitials (Zn_i) or
325 sulphur vacancy (V_s) (Peng et al. 2006). For the undoped ZnS NCs, the spectrum was
326 dominated by a band around 426 nm responsible for the blue luminescence originated from
327 sulfur vacancies V_s (Wang et al. 2011), while the yellow emission at 540 nm may be due to
328 interstitial zinc atom (I_{Zn}) (Phuong Nguyen et al. 2017). A new orange emission appeared at
329 580 nm when inserting Mn^{2+} ions into the crystal, which was attributed to ${}^4T_1 \rightarrow {}^6A_1$ transition
330 of Mn^{2+} ions (Tuan et al. 2018). The band at ~ 420 nm persisted and was related to radiative
331 carriers recombination between the sulphur vacancy sites (V_s) and the valence band (Mansur
332 and Mansur 2011). In terms of intensity, the luminescence of the orange emission band
333 increased with the doping level and reached a maximum emission for a concentration of 8%
334 Mn^{2+} . This result was associated to energy transfer from ZnS host matrix to Mn^{2+} ions due to
335 the strong coupling between the $3d^5$ electrons of Mn^{2+} ions and the ZnS p-electrons
336 (Kolmykov et al. 2014). At high doping concentration, the distance between Mn^{2+} ions
337 decreased and the dipole-dipole interaction between the electronic spins of two neighboring
338 Mn^{2+} ions was no longer negligible. Such coupling generated a reduction of the manganese

339 emission band with a slight red shift caused by a non-radiative cross-relaxation between these
340 ions (Fang et al. 2010). On the other hand, the decrement of the intensity of the overall
341 emission may be because Mn^{2+} ions settled at the superficial or interstitial positions of the
342 ZnS host. Some of these defects acted as non-radiative recombination centers in the host as
343 explained by Mohagheghpour et al.(Mohagheghpour et al. 2009). In order to provide a better
344 understanding of the different emission bands of Mn-doped ZnS NCs, an energy level
345 diagram was proposed where the possible radiative and non-radiative transitions of charge
346 carriers are illustrated, see *Figure 10*.

347 **3.3. MO dye adsorption and its analysis via advanced statistical physics model**

348 In recent years, II-VI semiconductors especially zinc sulfur (ZnS) have generated
349 considerable interest in wastewaters treatment due to their nontoxicity, physical and chemical
350 stability and high catalytic efficiency (Chang et al. 2017; Bujňáková et al. 2017; Ajibade et al.
351 2020). ZnS nano-adsorbents have advantages in terms of their abundance, low-cost, good
352 stability, non-toxicity and good light UV absorption. Therefore, they are considered suitable
353 for adsorption and photocatalysis applications. Herein, a simple colloidal chemical route for
354 the synthesis of undoped and Mn-doped ZnS nano-adsorbents using thioglycolic acid (TGA)
355 as a stabilizing agent is reported. This synthesis route offers a high purity, low-cost, simple
356 implementation and low energy consumption. The surface functionalization of nanocrystals
357 by TGA molecules modifies their adsorption activities, morphology, particle size, optical
358 properties and mechanical stability (Wieszczycka et al. 2021). It is worth noting that the
359 surface area and small particle size of ZnS contribute to enhance the adsorption efficiency.
360 Furthermore, the combination of adsorption and photocatalyst is an interesting approach to
361 degrade organic pollutants in wastewaters treatment.

362 *Figure 11* reports the adsorption kinetic of MO dye on undoped and Mn-doped ZnS nano-
363 adsorbent in dark conditions. Dye adsorption on the nano-adsorbent was fast for the first 5
364 min, then continued with a slower rate during 10-45 min and reached the equilibrium
365 condition after approximately 60 min. The experimental kinetic showed that doping with Mn
366 ions increased the MO adsorption capacity. Mn-doped ZnS NCs showed a better adsorption
367 than undoped ZnS NCs. This can be explained by the decrease in size under the effect of
368 doping, which generated an increase in the surface-to-volume ratio that provided more sites
369 on the surface. The pseudo second order kinetic rate equation (Mohamed et al. 2018; Bouzid
370 et al. 2019; Pang et al. 2020) was used to fit the experimental data (S 1898; Ho and McKay
371 1999; Pan et al. 2010; Ghasemi et al. 2014):

372

$$Q(t) = \frac{q_e^2 K_2 t}{1 + q_e K_2 t} \quad (8)$$

373 where K_2 (mg/gmin) is the pseudo second order rate constant of adsorption, q_e and $Q(t)$
374 (mg/g) are the adsorption capacity at equilibrium and time t , respectively. **Table 3** shows that
375 K_2 increased as a function of the Mn doping amount. Overall, the adsorption kinetic of MO on
376 undoped and Mn-doped ZnS nanocrystals could involve a rate limiting adsorption on the
377 vicinity of Mn-doped ZnS surface. This process can be associated to an exchange interaction
378 between MO and Mn-doped ZnS adsorbent surface. This interaction increased with Mn
379 doping in the ZnS.

380 On the other hand, the experimental isotherm showed that MO adsorption capacity of
381 undoped ZnS increased from 6.21 to 25.91 mg/g when the dye concentration also increased
382 from 10 to 50 mg/L, which corresponded to an adsorption efficiency of 64.56 %. However, the
383 Mn (12%)-doped ZnS NCs showed an adsorption efficiency of 71.16%, which proved that the
384 doping with manganese ions enhanced the adsorption. The adsorption capacity of undoped
385 and Mn-doped ZnS nanocrystals could be due to the ligand on the surface of inorganic TGA
386 particles, which could contribute with positively charged sites on the surface of ZnS due to
387 the zinc interstitials (Zn_i), Mn defects and sulfur vacancies (V_s) that were generated during the
388 synthesis (such as nonstoichiometric defects and dangling bonds). These sites generated
389 attraction forces with the negatively charged molecule of MO (with sulfonate group $R-SO_3^-$).
390 The adsorption mechanism of the MO molecule on ZnS adsorbent surface, with
391 different doping percentage of Mn, was analyzed with the Hill adsorption model obtained
392 from statistical physics. This model is presented in the Equation (9) (Bouzid et al. 2016, 2019;
393 Mohamed et al. 2018; Pang et al. 2020).

394

$$Q_a = \frac{n_D D_M}{\left(1 + \left(\frac{C_{1/2}}{C}\right)^{n_D}\right)} \quad (9)$$

395 where n_D is the number of MO molecules captured by the adsorption receptor site of adsorbent
396 surface, D_M is the density of receptor sites and $C_{1/2}$ is the concentration at half-saturation of
397 MO on the ZnS adsorbent surface with different doping of Mn. This last parameter can be
398 associated to the adsorption energy using the next expression (Bouzid et al. 2016, 2019;
399 Mohamed et al. 2018; Atrous et al. 2019; Pang et al. 2020; Bel Haj Mohamed et al. 2021;
400 Sghaier et al. 2021).

$$C_{1/2} = C_s e^{-\frac{\Delta E^a}{RT}} \quad (10)$$

where C_s is the MO dye solubility (i.e., 5.20 g/L). MO adsorption data were fitted with this model and their corresponding values are listed in **Table 4**, while the model fitting is illustrated in **Figure 12**.

Note that the parameter n_D can be used to describe the number of dyes adsorbed molecules per adsorption site and gives also information about the adsorption position. **Table 4** showed that $n_D=3.73$ indicating that MO dye molecules could be linked or adsorbed via a non-parallel orientation with a multi-molecular adsorption process. MO molecules can interact with the adsorbent surface thus forming an aggregate of three molecules per adsorption site of Mn-doped ZnS nanocrystals. Overall, n_D decreased with the increment of Mn amount in the ZnS host. Dye adsorption capacity at saturation was 25.31 mg/g and increased with the Mn doping. Mn in the ZnS NCs contributed to increase the specific adsorption surface of nanocrystals. The adsorption energy of MO on Mn-doped ZnS nanocrystals surface ranged from 22.47 to 23.47 kJ/mol thus corresponding to physical interactions like hydrogen bonding and van der Waals forces, see **Table 4**.

3.4 Photocatalytic activity

Figure 13 shows the absorption spectra of MO solutions using undoped and Mn-doped ZnS nanocatalysts for various contact times (0-120 min). The maximum absorption peak decreased with increasing irradiation time as a result of the reduction of MO dye concentration in the irradiated solution. It was observed the color disappearance after 6 min due to the breaking of the azo groups (N=N) responsible for the orange coloration, which indicated that the aromatic compounds were attacked by hydroxyl radicals forming radical intermediates (Chan et al. 2011). These experiments demonstrated the high photocatalytic efficiency of pure ZnS NCs, which generated a rapid degradation of MO molecules and the solution decolorization.

To quantify the photocatalytic activity of ZnS NCs, the degradation efficiency, degradation constant and half-life were calculated using the following equations (Dhandapani et al. 2016):

$$\eta = \frac{(A_0 - A_t)}{A_0} \times 100 = \frac{(C_0 - C_t)}{C_0} \times 100 \quad (11)$$

$$Kt = \ln \left(\frac{A_0}{A_t} \right) = \ln \left(\frac{C_0}{C_t} \right) \quad (12)$$

$$t_{1/2} = \frac{\ln(2)}{k} \quad (13)$$

430 where A_0 , A_t , C_0 and C_t are the initial absorbance, the absorbance after irradiation, the initial
431 concentration of the solution and the concentration of the dye after irradiation for time t ,
432 respectively.

433 The values of degradation efficiency of undoped ZnS NCs are given in Table 5. These results
434 revealed a high degradation efficiency of MO after just 6 min of irradiation (~81.4 %). After
435 120 min of irradiation, the degradation efficiency was 98.5% and the solution became
436 uncolored. This high efficiency may be due to the small size of the TGA molecules used as
437 stabilizer in addition to the largest specific surface of NCs, thus generating several available
438 adsorption sites.

439 The effect of manganese doping on the photocatalytic activity of MO is illustrated in Figure
440 13. The solution decolorization was obtained at higher contact time than that observed with
441 the undoped ZnS NCs. Table 6 showed that doping generated an impeding effect for the MO
442 degradation and the corresponding efficiency was lower than that observed using undoped
443 ZnS. The highest MO degradation efficiency was obtained for 8% manganese concentration
444 of doped ZnS NCs. In terms of degradation time, this doping concentration of ZnS NCs
445 required 120 min for obtaining an efficiency of 87.1%.

446 The pseudo-first-order kinetic equation was used to calculate the rate constant (k) for MO
447 degradation using pure and Mn doped ZnS NCs where the corresponding plots of $\ln(A_0/A_t)$
448 versus irradiation time are given in Figure 14. The rate constants ranged from 0.281 to 0.004
449 min^{-1} , see Table 6. Indeed, the trapping of charge carriers with pure ZnS was provided by
450 sulfur vacancies, while multiple traps of charge carriers occurred with manganese doped ZnS
451 due to structural defects in ZnS NCs (i.e., vacancies and interstices of Zn and S, interstices of
452 Mn) and other surface defects (Zong et al. 2014). These defects produced discrete energy
453 levels within the forbidden band (E_g) of ZnS NPs and, therefore, the possibility of
454 recombination of electron and hole inside the NPs increased (Štengl et al. 2009), which
455 resulted in a reduction of the photocatalytic activity of these NCs with low MO degradation.
456 In view of that, it has been suggested that as the concentration of Mn^{2+} ions increased, a
457 competitive process of charge carrier trapping between V_s and Mn^{2+} occurred (Sergeeva et al.
458 2018).

459 The rate of MO degradation depended on nanocatalyst properties such as specific surface,
460 nanocrystal size, composition, crystallinity and gap energy (Chaturvedi et al. 2012). Despite
461 the photoluminescence, properties of ZnS were ameliorated via Mn^{2+} doping thus reaching a

462 maximum for 8% ZnS, results showed that a low MO degradation was obtained with doped
463 NCs. This finding can be explained by the high probability of electron-hole recombination for
464 doped NCs and, subsequently, the strong PL response impacted indirectly on photocatalytic
465 activity by the low density of free excitons that migrate to the surface where they generated
466 oxidizing species(Ashkarran 2014). As a result, the presence of high photoluminescence
467 generated a low photocatalytic activity. Consequently, undoped ZnS NCs are a promising
468 nanocatalyst for the degradation of MO dye and its application can be extended to degrade
469 other organic molecules.

470 **3.5. Toward an industrial efficient solar activated nanocatalyst**

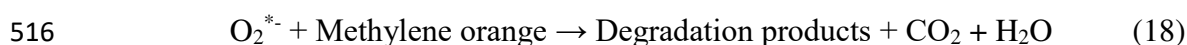
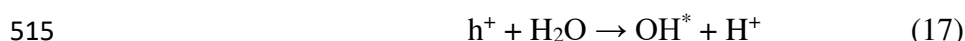
471 As stated, the degradation of organic pollutants is a necessity due to environmental pollution
472 problems. Consequently, the industries request the most efficient degradation process but with
473 a low cost. One way to achieve this goal is the use of solar activated efficient photocatalyst. In
474 this context, additional photodegradation experiments were carried out under solar light
475 irradiation to evaluate the usability of undoped ZnS NCs for wastewater purification. Before
476 the sunlight irradiation, the suspensions were magnetically stirred for 120 min to allow
477 adsorption-desorption equilibrium between MO molecules and NCs. Then, the mixture was
478 submitted to sunlight irradiation between 11 am and 2 pm to evaluate the dye degradation.
479 Figure 15 presents the UV-visible absorption spectra of MO degradation using ZnS NCs and
480 the degradation rate as a function of time recorded after sunlight exposition. Results of Figure
481 15 and Table 7showed the total decolorization of the solution after 120 min of sunlight
482 exposition. This experiment confirmed the degradation efficiency of these NCs. Overall, the
483 percentage of dye degradation increased significantly with the exposition time where 97.4%
484 was the maximum decolorization efficiency with a degradation constant K of 0.045 min^{-1} . In
485 fact, there was no a significant difference with the efficiency obtained under UV irradiation
486 (98.5%). It is convenient to note that sunlight is often exploited for
487 thesemiconductorsirradiation with the aim of performing the photodegradation of pollutants
488 thus contributing to reduce the cost of water treatment methods and the environmental
489 pollution as compared to UV lamps. These results proved that undoped ZnS NCs exhibited a
490 strong photocatalytic activity for MO dye. This behavior may be explained by the large band
491 gap energy of ZnS, which caused a higher redox potential of e-h pairs and, consequently, a
492 higher photocatalytic performance (Herrmann et al. 1984). The photocatalytic efficiency of
493 ZnS NCs was compared with other nanocatalysts reported in the literature and the results are
494 summarized in Table 8. It is clear that pure ZnS can be a good candidate for dye degradation

495 under sunlight irradiation. This material offer additional advantages such as it does not use
496 expensive organic moieties and toxic products in the catalyst preparation together with a
497 higher rate of decolorization under UV and sunlight irradiations(Gajendiran et al. 2020; Samanta
498 et al. 2018; Pathania et al. 2016; Suganya et al. 2019; Samanta et al. 2020; Dake et al. 2020; Ramki et
499 al. 2020; Matras-Postolek et al. 2019).These results are encouraging for the application of these
500 NCs to degrade organic compounds dissolved in wastewater at great scale in the industrial
501 sector.

502 3.4. Mechanism of photocatalytic activity

503 The mechanism of photocatalytic degradation of methylene orange by undoped and doped
504 ZnS nanocatalysts could be explained as follows. First, UV light excitation of ZnS NCs
505 generated the electron-hole pairs (e^-/h^+) in ZnS. The (OH^*) radical was formed from a simple
506 oxidation of water or hydroxyl ion (OH^-) by photo-generated holes. Similarly, superoxide
507 radicals (O_2^{*-}) were formed in water from a reduction reaction of the dissolved dioxygen in
508 water by photo-generated electrons. These highly reactive hydroxyl radicals (OH^*) and
509 superoxide radicals (O_2^{*-}) reacted with MO dye molecule adsorbed on ZnS nanoparticles
510 ensuring the degradation. The next equations describe this mechanism

511



518 Figure 16 summarizes the different stages of this photocatalytic process. The first step
519 corresponded to the transfer of the MO molecule from the aqueous phase to the surface of
520 NCs. In the second step, the organic molecules were adsorbed on the surface of the catalyst
521 followed by the movement of photo-generated e^- and h^+ charges to the catalyst surface. The
522 positive hole in the NCs reacted with a water molecule to produce hydrogen gas and free
523 hydroxyl radical (OH^*), which was the most important and powerful oxidizing radical for the
524 mineralization of adsorbed or free MO on the catalyst surface. Photo-induced electrons were
525 easily trapped by electronic acceptors, such as adsorbed O_2 , to produce a super oxide anion
526 radical (O_2^{*-}). This reaction limited the recombination phenomena and thus improved

527 degradation efficiency. Finally, these different radicals reacted with the MO to form
528 intermediate compounds before the mineralization to CO₂ and H₂O.

529 **4. Conclusions**

530 Nanocrystals of undoped and Mn-doped ZnS were successfully synthesized by colloidal
531 precipitation reaction method and applied in the photodegradation of MO dye. FTIR results
532 confirmed the functionalization of nanocrystals surface by TGA. XRD analysis indicated the
533 formation of nanocrystals with two crystalline phases, hexagonal and cubic, identical to the
534 solid material and with a relatively large size distribution. The average size of ZnS
535 nanocrystals calculated by using Debye-Scherrer formula varied from 2.5 to 7.1 nm. The
536 optical absorption spectra showed the appearance of an absorption edge shifted towards short
537 wavelengths compared to that of the solid-state semiconductor ZnS. PL spectroscopy
538 indicated that the emission intensity increased with the doping rate up to 8% and then it
539 decreased. Modeling results showed that the Hill model explained the adsorption mechanism
540 of MO on the nanocrystal surface, dye removal followed a pseudo-second order reaction
541 kinetics. Adsorption capacity of doped ZnS-TGA was 26.98 mg/g and this property
542 contributed to the direct interaction of photo-generated electrons with adsorbed MO
543 molecules and hence facilitated a quick photodegradation. Dye adsorption process was multi-
544 molecular via physisorption involving hydrogen bonding and van der Waals interactions. The
545 undoped ZnS-TGA nanocrystals exhibited high photocatalytic activity to degrade MO dye
546 under UV and sunlight. Consequently, the pure ZnS-TGA nanocatalysts are suggested as a
547 promising photocatalyst for wastewater purification. On the other hand, Mn-doped ZnS-TGA
548 nanocrystals showed superior optical and physicochemical characteristics making them good
549 candidates for fluorescence-based applications.

550

551 **Author's contribution:**

552 **Sabri Ouni:** Writing - original draft, Visualization, Conceptualization, Methodology

553 **Naim Bel Haj Mohamed:** Visualization, Writing – review & editing; Conceptualization,
554 Methodology

555 **Noureddine Chaaben:** Resources, Writing – review & editing

556 **Adrian Bonilla-Petriciolet:** Writing - Reviewing and Editing

557 **Mohamed Haouari:** Writing - Reviewing and Editing, Visualization, Supervision

558

559 **Funding:**

560 The authors declare that they have no known competing financial interests or personal
561 relationships that could have appeared to influence the work reported in this paper.

562 **Availability of data and materials:** Data and materials are contained within the article

563 **Declarations**

564 **Ethics approval and consent to participate:** Not applicable for this study.

565 **Consent to publish:** All authors consent to this publication.

566 **Competing interests:** The authors declare no competing interests

567

568

569

570

571

572

573

574

575

576

577

578

579

580

581

582

583

584

585

586

587

588

589

590

591

592

593

594 **References**

- 595 Ajibade PA, Oluwalana AE, Sikakane BM, Singh M (2020) Structural, photocatalytic and anticancer
596 studies of hexadecylamine capped ZnS nanoparticles. *Chem Phys Lett* 755:137813.
597 <https://doi.org/10.1016/j.cplett.2020.137813>
- 598 Amaranatha Reddy D, Liu C, Vijayalakshmi RP, Reddy BK (2014) Effect of Al doping on the structural,
599 optical and photoluminescence properties of ZnS nanoparticles. *J Alloys Compd* 582:257–264.
600 <https://doi.org/10.1016/j.jallcom.2013.08.051>
- 601 Amirian F, Molaei M, Karimipour M, Bahador AR (2018) A new and simple UV-assisted approach for
602 synthesis of water soluble ZnS and transition metals doped ZnS nanoparticles (NPs) and investigating
603 optical and photocatalyst properties. *J Lumin* 196:174–180.
604 <https://doi.org/10.1016/j.jlumin.2017.12.005>
- 605 Arao Y, Hirooka Y, Tsuchiya K, Mori Y (2009) Structure and Photoluminescence Properties of Zinc
606 Sulfide Nanoparticles Prepared in a Clay Suspension. *J Phys Chem C* 113:894–899.
607 <https://doi.org/10.1021/jp8051449>
- 608 Ashkarran AA (2014) Absence of photocatalytic activity in the presence of the photoluminescence
609 property of Mn–ZnS nanoparticles prepared by a facile wet chemical method at room temperature.
610 *Mater SciSemicond Process* 17:1–6. <https://doi.org/10.1016/j.mssp.2013.08.003>
- 611 Atrous M, Sellaoui L, Bouzid M, et al (2019) Adsorption of dyes acid red 1 and acid green 25 on
612 grafted clay: Modeling and statistical physics interpretation. *J Mol Liq* 294:111610.
613 <https://doi.org/10.1016/j.molliq.2019.111610>
- 614 Bel Haj Mohamed N, Bouzidi M, Ben brahim N, et al (2021) Impact of the stacking fault and surface
615 defects states of colloidal CdSe nanocrystals on the removal of reactive black 5. *Mater SciEng B*
616 265:115029. <https://doi.org/10.1016/j.mseb.2020.115029>
- 617 Bouzid M, Bouaziz N, Torkia YB, Lamine AB (2019) Statistical physics modeling of ethanol adsorption
618 onto the phenol resin based adsorbents: Stereographic, energetic and thermodynamic investigations.
619 *J Mol Liq* 283:674–687. <https://doi.org/10.1016/j.molliq.2019.03.129>
- 620 Bouzid M, Sellaoui L, Khalfaoui M, et al (2016) Adsorption of ethanol onto activated carbon:
621 Modeling and consequent interpretations based on statistical physics treatment. *Phys Stat Mech Its*
622 *Appl* 444:853–869. <https://doi.org/10.1016/j.physa.2015.09.097>
- 623 Brus L (1986) Electronic wave functions in semiconductor clusters: experiment and theory. *J Phys*
624 *Chem* 90:2555–2560. <https://doi.org/10.1021/j100403a003>
- 625 Bujňáková Z, Dutková E, Kello M, et al (2017) Mechanochemistry of Chitosan-Coated Zinc Sulfide
626 (ZnS) Nanocrystals for Bio-imaging Applications. *Nanoscale Res Lett* 12:328.
627 <https://doi.org/10.1186/s11671-017-2103-z>
- 628 Buthiyappan A, Aziz ARA, Daud WMAW (2016) Recent advances and prospects of catalytic advanced
629 oxidation process in treating textile effluents. *Rev ChemEng* 32:1–47. [https://doi.org/10.1515/revce-](https://doi.org/10.1515/revce-2015-0034)
630 2015-0034

631 Chan SHS, Wu TY, Juan JC, Teh CY (2011) Recent developments of metal oxide semiconductors as
632 photocatalysts in advanced oxidation processes (AOPs) for treatment of dye waste-water. J
633 ChemTechnolBiotechnol 86:1130–1158. <https://doi.org/10.1002/jctb.2636>

634 Chang L, He X, Chen L, Zhang Y (2017) Mercaptophenylboronic acid-capped Mn-doped ZnS quantum
635 dots for highly selective and sensitive fluorescence detection of glycoproteins. Sens Actuators B
636 Chem 243:72–77. <https://doi.org/10.1016/j.snb.2016.11.121>

637 Chaturvedi S, Dave PN, Shah NK (2012) Applications of nano-catalyst in new era. J Saudi ChemSoc
638 16:307–325. <https://doi.org/10.1016/j.jscs.2011.01.015>

639 Chauhan R, Kumar A, Pal Chaudhary R (2014) Photocatalytic degradation of methylene blue with Cu
640 doped ZnS nanoparticles. J Lumin 145:6–12. <https://doi.org/10.1016/j.jlumin.2013.07.005>

641 Dake DV, Raskar ND, Mane VA, et al (2020) Exploring the role of defects on diverse properties of Cr-
642 substituted ZnS nanostructures for photocatalytic applications. Appl Phys A 126:640.
643 <https://doi.org/10.1007/s00339-020-03669-1>

644 Dao V-D (2020) Bimetallic PtSe nanoparticles incorporating with reduced graphene oxide as efficient
645 and durable electrode materials for liquid-junction photovoltaic devices. Mater Today Energy
646 16:100384. <https://doi.org/10.1016/j.mtener.2020.100384>

647 Daskalakis I, Vamvasakis I, T. Papadas I, et al (2020) Surface defect engineering of mesoporous
648 Cu/ZnS nanocrystal-linked networks for improved visible-light photocatalytic hydrogen production.
649 InorgChem Front 7:4687–4700. <https://doi.org/10.1039/D0QI01013H>

650 Dehghan F, Molaei M, Amirian F, et al (2018) Improvement of the optical and photocatalytic
651 properties of ZnSe QDs by growth of ZnS shell using a new approach. Mater Chem Phys 206:76–84.
652 <https://doi.org/10.1016/j.matchemphys.2017.11.061>

653 Dhandapani C, Narayanasamy R, Karthick SN, et al (2016) Drastic photocatalytic degradation of
654 methylene blue dye by neodymium doped zirconium oxide as photocatalyst under visible light
655 irradiation. Optik 127:10288–10296. <https://doi.org/10.1016/j.ijleo.2016.08.048>

656 Fang Z, Wu P, Zhong X, Yang Y-J (2010) Synthesis of highly luminescent Mn:ZnSe/ZnS nanocrystals in
657 aqueous media. Nanotechnology 21:305604. <https://doi.org/10.1088/0957-4484/21/30/305604>

658 Gaceur M, Giraud M, Hemadi M, et al (2012) Polyol-synthesized Zn_{0.9}Mn_{0.1}S nanoparticles as
659 potential luminescent and magnetic bimodal imaging probes: synthesis, characterization, and toxicity
660 study. J Nanoparticle Res 14:932. <https://doi.org/10.1007/s11051-012-0932-3>

661 Gajendiran J, Gnanam S, Vijaya Kumar V, et al (2020) Structural, optical and photocatalytic properties
662 of ZnS spherical/flake nanostructures by sugar-assisted hydrothermal process. Chem Phys Lett
663 754:137639. <https://doi.org/10.1016/j.cplett.2020.137639>

664 Ghasemi M, Ghasemi N, Zahedi G, et al (2014) Kinetic and equilibrium study of Ni(II) sorption from
665 aqueous solutions onto Peganumharmala-L. Int J Environ SciTechnol 11:1835–1844.
666 <https://doi.org/10.1007/s13762-014-0617-9>

667 Herrmann J-M, Disdier J, Pichat P (1984) Effect of chromium doping on the electrical and catalytic
668 properties of powder titania under UV and visible illumination. Chem Phys Lett 108:618–622.
669 [https://doi.org/10.1016/0009-2614\(84\)85067-8](https://doi.org/10.1016/0009-2614(84)85067-8)

670 Ho YS, McKay G (1999) Pseudo-second order model for sorption processes. *Process Biochem* 34:451–
671 465. [https://doi.org/10.1016/S0032-9592\(98\)00112-5](https://doi.org/10.1016/S0032-9592(98)00112-5)

672 Jai Kumar B, Mahesh HM (2017) Concentration-dependent optical properties of TGA stabilized CdTe
673 Quantum dots synthesized via the single injection hydrothermal method in the ambient
674 environment. *SuperlatticesMicrostruct* 104:118–127. <https://doi.org/10.1016/j.spmi.2017.02.023>

675 Jaldurgam FF, Ahmad Z, Touati F (2021) Synthesis and Performance of Large-Scale Cost-Effective
676 Environment-Friendly Nanostructured Thermoelectric Materials. *Nanomaterials* 11:1091.
677 <https://doi.org/10.3390/nano11051091>

678 Jothibas M, Manoharan C, Johnson Jeyakumar S, et al (2018) Synthesis and enhanced photocatalytic
679 property of Ni doped ZnS nanoparticles. *Sol Energy* 159:434–443.
680 <https://doi.org/10.1016/j.solener.2017.10.055>

681 Jothibas M, Manoharan C, Johnson Jeyakumar S, et al (2016) Photocatalytic activity of spray
682 deposited ZrO₂ nano-thin films on methylene blue decolouration. *J Mater Sci Mater Electron*
683 27:5851–5859. <https://doi.org/10.1007/s10854-016-4502-9>

684 Kabachii YA, KochevSYu, AntonovaOYu, et al (2021) Mn²⁺-doped ZnS–CdS alloy nanocrystals for the
685 photocatalytic hydrogen evolution reaction. *Mendeleev Commun* 31:315–318.
686 <https://doi.org/10.1016/j.mencom.2021.04.012>

687 Kaur J, Sharma M, Pandey OP (2015) Photoluminescence and photocatalytic studies of metal ions
688 (Mn and Ni) doped ZnS nanoparticles. *Opt Mater* 47:7–17.
689 <https://doi.org/10.1016/j.optmat.2015.06.022>

690 Kolmykov O, Coulon J, Lalevée J, et al (2014) Aqueous synthesis of highly luminescent glutathione-
691 capped Mn²⁺-doped ZnS quantum dots. *Mater SciEng C* 44:17–23.
692 <https://doi.org/10.1016/j.msec.2014.07.064>

693 Kostrov AN, Gostev FE, Shelaev IV, et al (2020) Relaxation Dynamics of Excited States in Mn²⁺-Doped
694 ZnCdS (Core)/ZnS (Shell) Quantum Dots Ions in Propylene Carbonate. *High Energy Chem* 54:421–426.
695 <https://doi.org/10.1134/S0018143920060090>

696 Li W, Ju B, Zhang S (2019) A green l -cysteine modified cellulose nanocrystals biosorbent for
697 adsorption of mercury ions from aqueous solutions. *RSC Adv* 9:6986–6994.
698 <https://doi.org/10.1039/C9RA00048H>

699 Liu I-S, Lo H-H, Chien C-T, et al (2008) Enhancing photoluminescence quenching and photoelectric
700 properties of CdSe quantum dots with hole accepting ligands. *J Mater Chem* 18:675–682.
701 <https://doi.org/10.1039/B715253A>

702 Long F, Ning S, Zhang W, et al (2020) All-fiber passively Q-switched erbium-doped laser with
703 Cr²⁺:ZnSe nanocrystals saturable absorber. *Laser Phys* 30:055101.
704 <https://doi.org/10.1088/1555-6611/ab8233>

705 Mansur HS, Mansur AAP (2011) CdSe quantum dots stabilized by carboxylic-functionalized PVA:
706 Synthesis and UV–vis spectroscopy characterization. *Mater Chem Phys* 125:709–717.
707 <https://doi.org/10.1016/j.matchemphys.2010.09.068>

708 Matras-Postołek K, Sovinska S, Węgrzynowicz A (2019) Synthesis and characterization of ZnSe and
709 ZnSe:Mn nanosheets and microflowers with high photoactive properties by microwave-assisted

710 method. *ChemEng Process - Process Intensif* 135:204–216.
711 <https://doi.org/10.1016/j.cep.2018.11.022>

712 Meikle TG, Dyett BP, Strachan JB, et al (2020) Preparation, Characterization, and Antimicrobial
713 Activity of Cubosome Encapsulated Metal Nanocrystals. *ACS Appl Mater Interfaces* 12:6944–6954.
714 <https://doi.org/10.1021/acsami.9b21783>

715 Meng L, Maçarico A, Martins R (1995) Study of annealed indium tin oxide films prepared by rf
716 reactive magnetron sputtering. *Vacuum* 46:673–680. [https://doi.org/10.1016/0042-207X\(94\)00150-2](https://doi.org/10.1016/0042-207X(94)00150-2)

717 Mohaghehpour E, Rabiee M, Moztafzadeh F, et al (2009) Controllable synthesis, characterization
718 and optical properties of ZnS:Mn nanoparticles as a novel biosensor. *Mater SciEng C* 29:1842–1848.
719 <https://doi.org/10.1016/j.msec.2009.02.012>

720 Mohamed B, Qingyu Z, D. Moggridge G, Abdelmottaleb BL (2018) New insight in adsorption of
721 pyridine on the two modified adsorbents types MN200 and MN500 by means of grand canonical
722 ensemble. *J Mol Liq* 263:413–421. <https://doi.org/10.1016/j.molliq.2018.05.008>

723 Mote VD, Purushotham Y, Dole BN (2013) Structural, morphological and optical properties of Mn
724 doped ZnS nanocrystals. 6

725 Nath D, Singh F, Das R (2020) X-ray diffraction analysis by Williamson-Hall, Halder-Wagner and size-
726 strain plot methods of CdSe nanoparticles- a comparative study. *Mater Chem Phys* 239:122021.
727 <https://doi.org/10.1016/j.matchemphys.2019.122021>

728 Othman AA, Osman MA, Ali MA, et al (2020) Sonochemically synthesized Ni-doped ZnS nanoparticles:
729 structural, optical, and photocatalytic properties. *J Mater Sci Mater Electron* 31:1752–1767.
730 <https://doi.org/10.1007/s10854-019-02693-z>

731 Ouni S, Bel Haj Mohamed N, Bouzidi M, et al (2021) High impact of thiol capped ZnS nanocrystals on
732 the degradation of single and binary aqueous solutions of industrial azo dyes under sunlight. *J*
733 *Environ ChemEng* 9:105915. <https://doi.org/10.1016/j.jece.2021.105915>

734 Pan B, Sun K, Xing B (2010) Adsorption kinetics of 17 α -ethinyl estradiol and bisphenol A on carbon
735 nanomaterials. II. Concentration-dependence. *J SoilsSediments* 10:845–854.
736 <https://doi.org/10.1007/s11368-009-0185-7>

737 Pandya SG, Corbett JP, Jadwisieniczak WM, Kordesch ME (2016) Structural characterization and X-ray
738 analysis by Williamson–Hall method for Erbium doped Aluminum Nitride nanoparticles, synthesized
739 using inert gas condensation technique. *Phys E Low-DimensSyst Nanostructures* 79:98–102.
740 <https://doi.org/10.1016/j.physe.2015.12.013>

741 Pang X, Bouzid M, dos Santos JMN, et al (2020) Theoretical study of indigotine blue dye adsorption
742 on CoFe₂O₄/chitosan magnetic composite via analytical model. *Colloids Surf PhysicochemEng Asp*
743 589:124467. <https://doi.org/10.1016/j.colsurfa.2020.124467>

744 Pathania D, Gupta D, Al-Muhtaseb AH, et al (2016) Photocatalytic degradation of highly toxic dyes
745 using chitosan-g-poly(acrylamide)/ZnS in presence of solar irradiation. *J Photochem Photobiol Chem*
746 329:61–68. <https://doi.org/10.1016/j.jphotochem.2016.06.019>

747 Pejjai B, Minnam Reddy VR, Seku K, et al (2017) Chemical bath deposition of Mn-doped ZnS thin films
748 using greener complexing agents: Effect of Mn-doping on the optical properties. *Optik* 130:608–618.
749 <https://doi.org/10.1016/j.ijleo.2016.10.083>

750 Peng WQ, Cong GW, Qu SC, Wang ZG (2006) Synthesis and photoluminescence of ZnS:Cu
751 nanoparticles. *Opt Mater* 29:313–317. <https://doi.org/10.1016/j.optmat.2005.10.003>

752 Phuong Nguyen T, Duy Le A, Bich Vu T, Vinh Lam Q (2017) Investigations on photoluminescence
753 enhancement of poly(vinylalcohol)-encapsulated Mn-doped ZnS quantum dots. *J Lumin* 192:166–
754 172. <https://doi.org/10.1016/j.jlumin.2017.06.031>

755 Poornaprakash B, Chalapathi U, Suh Y, et al (2018) Terbium-doped ZnS quantum dots: Structural,
756 morphological, optical, photoluminescence, and photocatalytic properties. *Ceram Int* 44:11724–
757 11729. <https://doi.org/10.1016/j.ceramint.2018.03.250>

758 Ramki K, RajaPriya A, Sakthivel P, et al (2020) Rapid degradation of organic dyes under sunlight using
759 tin-doped ZnS nanoparticles. *J Mater Sci Mater Electron* 31:8750–8760.
760 <https://doi.org/10.1007/s10854-020-03410-x>

761 Rtimi S, Kiwi J, Nadtochenko V (2021) Photo-induced environmental remediation, biomedical
762 imaging, and microbial inactivation by Mn-doped semiconductors: critical issues. *Curr Opin Chem Eng*
763 34:100731. <https://doi.org/10.1016/j.coche.2021.100731>

764 S L (1898) ABOUT THE THEORY OF SO-CALLED ADSORPTION OF SOLUBLE SUBSTANCES. 24:1–39

765 Saenger DU, Jung G, Menning M (1998) Optical and Structural Properties of Doped ZnS Nanoparticles
766 Produced by the Sol-Gel Method. *J Sol-Gel Sci Technol* 13:635–639.
767 <https://doi.org/10.1023/A:1008663831823>

768 Samanta D, Basnet P, InakhunbiChanu T, Chatterjee S (2020) Biomolecule assisted morphology-
769 controllable synthesis of Zinc Sulphide nanomaterials for efficient photocatalytic activity under solar
770 irradiation. *J Alloys Compd* 844:155810. <https://doi.org/10.1016/j.jallcom.2020.155810>

771 Samanta D, Chanu TI, Basnet P, Chatterjee S (2018) Organic Dye Degradation Under Solar Irradiation
772 by Hydrothermally Synthesized ZnS Nanospheres. *J Mater Eng Perform* 27:2673–2678.
773 <https://doi.org/10.1007/s11665-018-3214-0>

774 Sergeeva KA, Sergeev AA, Kuznetsova YV, Voznesenskiy SS (2018) ZnS:Mn²⁺ Quantum Dots as
775 Efficient Photocatalyst for Organic Dye Decolorization. *Defect Diffus Forum* 386:207–213.
776 <https://doi.org/10.4028/www.scientific.net/DDF.386.207>

777 Sghaier W, Ben Torkia Y, Bouzid M, Ben Lamine A (2021) CO₂ adsorption investigation by statistical
778 physics: Thermodynamic analysis for cooling cycle application. *J Environ Chem Eng* 9:105108.
779 <https://doi.org/10.1016/j.jece.2021.105108>

780 Singh V, Chauhan P (2009) Structural and optical characterization of CdS nanoparticles prepared by
781 chemical precipitation method. *J Phys Chem Solids* 70:1074–1079.
782 <https://doi.org/10.1016/j.jpcs.2009.05.024>

783 Štengl V, Bakardjieva S, Murafa N (2009) Preparation and photocatalytic activity of rare earth doped
784 TiO₂ nanoparticles. *Mater Chem Phys* 114:217–226.
785 <https://doi.org/10.1016/j.matchemphys.2008.09.025>

786 Su D, Wang L, Li M, et al (2020) Highly luminescent water-soluble AgInS₂/ZnS quantum dots-hydrogel
787 composites for warm white LEDs. *J Alloys Compd* 824:153896.
788 <https://doi.org/10.1016/j.jallcom.2020.153896>

789 Suganya S, Jothibas M, Jeyakumar SJ (2019) Solid state synthesis of cadmium doped ZnS with
790 excellent photocatalytic activity and enhanced visible light emission. *J Mater Sci Mater Electron*
791 30:7916–7927. <https://doi.org/10.1007/s10854-019-01113-6>

792 Tuan NT, Trung DQ, Quang NV, et al (2018) Excitation energy dependence of the life time of orange
793 emission from Mn-doped ZnS nanocrystals. *J Lumin* 199:39–44.
794 <https://doi.org/10.1016/j.jlumin.2018.02.062>

795 Wang L, Wang P, Huang B, et al (2017) Synthesis of Mn-doped ZnS microspheres with enhanced
796 visible light photocatalytic activity. *Appl Surf Sci* 391:557–564.
797 <https://doi.org/10.1016/j.apsusc.2016.06.159>

798 Wang X, Shi J, Feng Z, et al (2011) Visible emission characteristics from different defects of ZnS
799 nanocrystals. *Phys ChemChem Phys* 13:4715–4723. <https://doi.org/10.1039/C0CP01620A>

800 Wieszczycka K, Staszak K, Woźniak-Budych MJ, et al (2021) Surface functionalization – The way for
801 advanced applications of smart materials. *CoordChem Rev* 436:213846.
802 <https://doi.org/10.1016/j.ccr.2021.213846>

803 Xie R, Li L, Li Y, et al (2011) Fe:ZnSe semiconductor nanocrystals: Synthesis, surface capping, and
804 optical properties. *J Alloys Compd* 509:3314–3318. <https://doi.org/10.1016/j.jallcom.2010.12.046>

805 Yang L, Zhou H, Fan T, Zhang D (2014) Semiconductor photocatalysts for water oxidation: current
806 status and challenges. *Phys ChemChem Phys* 16:6810–6826. <https://doi.org/10.1039/C4CP00246F>

807 Zong Y, Li Z, Wang X, et al (2014) Synthesis and high photocatalytic activity of Eu-doped ZnO
808 nanoparticles. *Ceram Int* 40:10375–10382. <https://doi.org/10.1016/j.ceramint.2014.02.123>

809

810

Figures

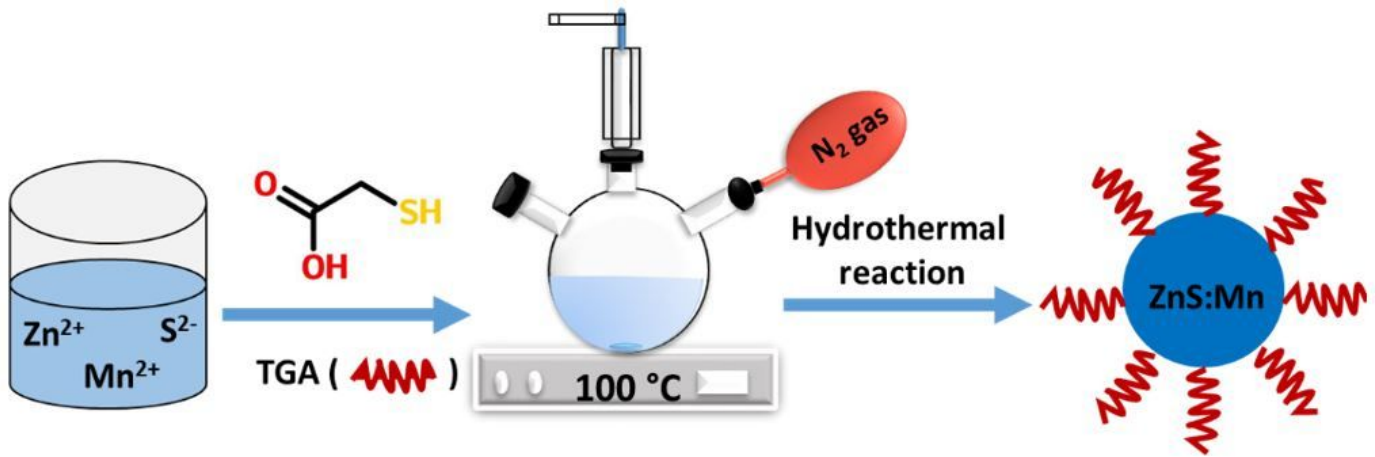


Figure 1

Description of synthesis protocol to obtain Mn-doped ZnS-TGA nanocrystals.

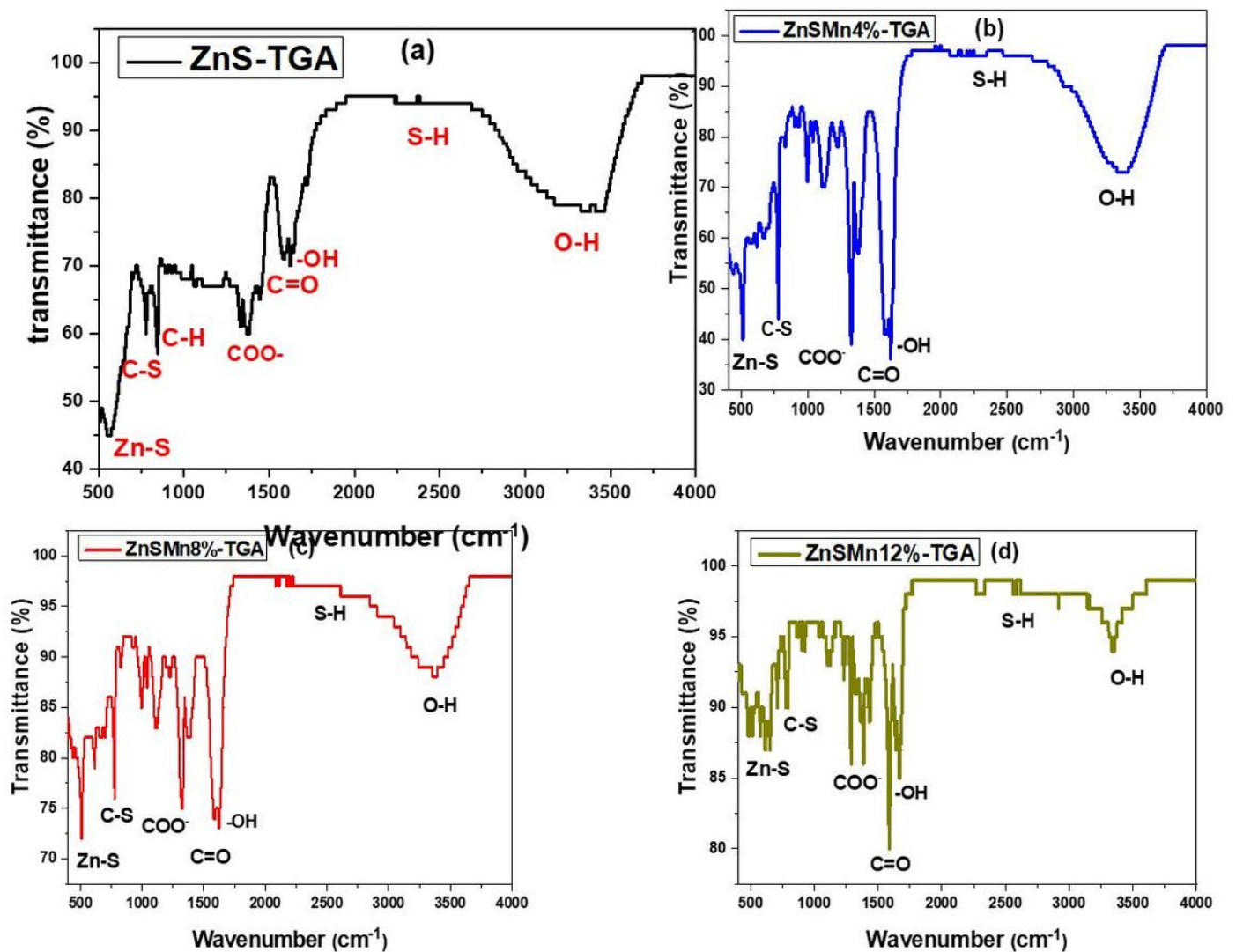


Figure 2

FTIR spectra of (a) undoped and Mn-doped ZnS-TGA nanocrystals with doping of (b) 4%, (c) 8% and (d) 12%.

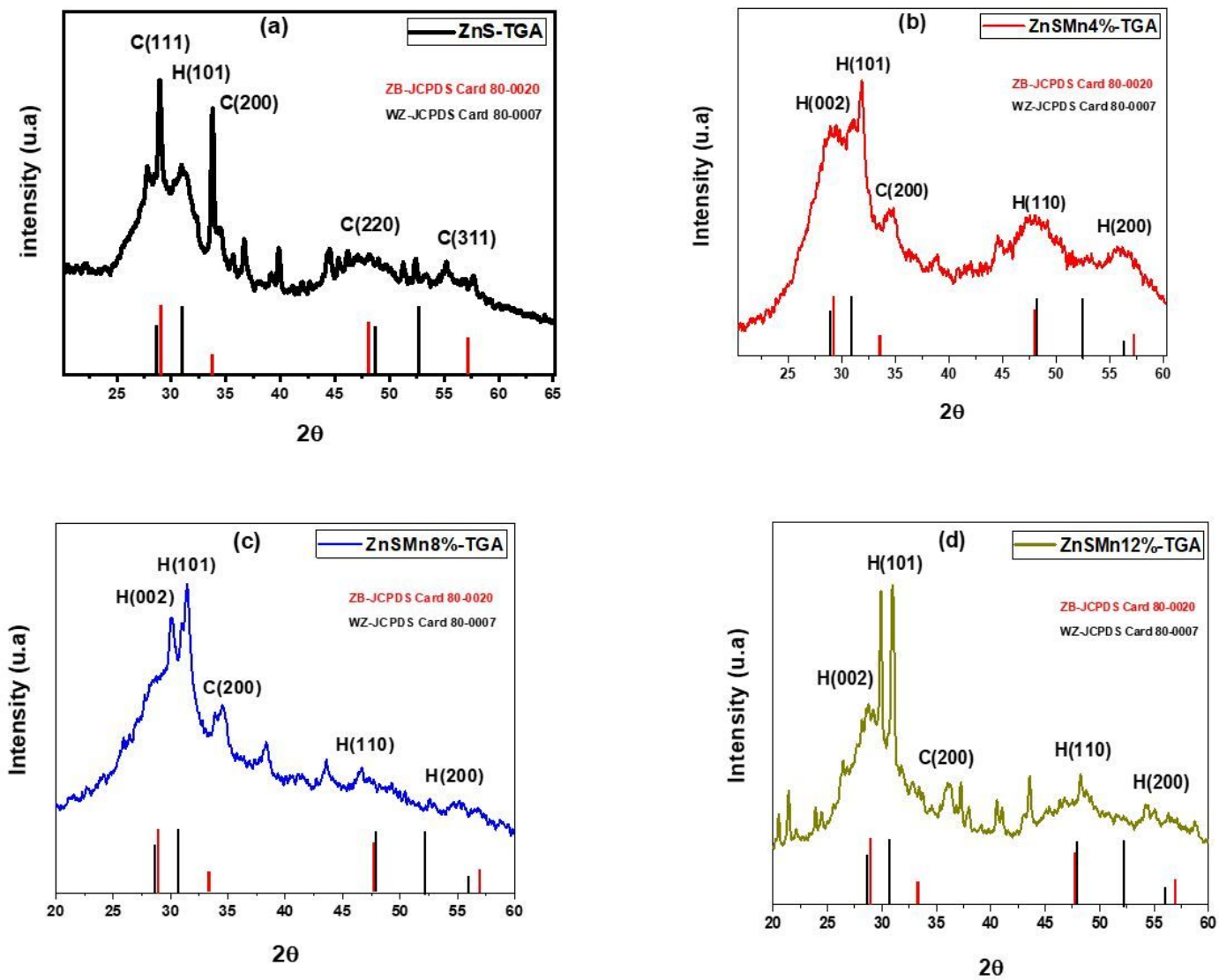


Figure 3

DRX patterns of undoped and Mn-doped ZnS-TGA nanocrystals.

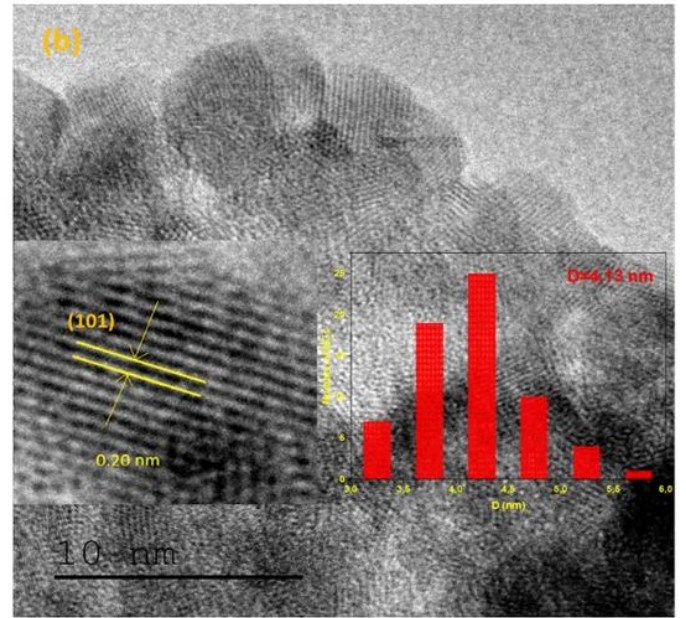
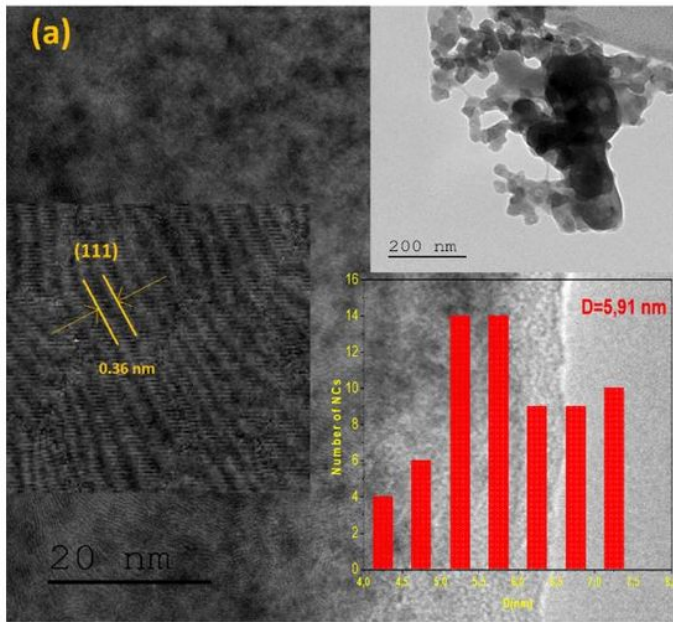


Figure 4

TEM images of (a) undoped and (b) Mn-doped ZnS-TGA nanocrystals.

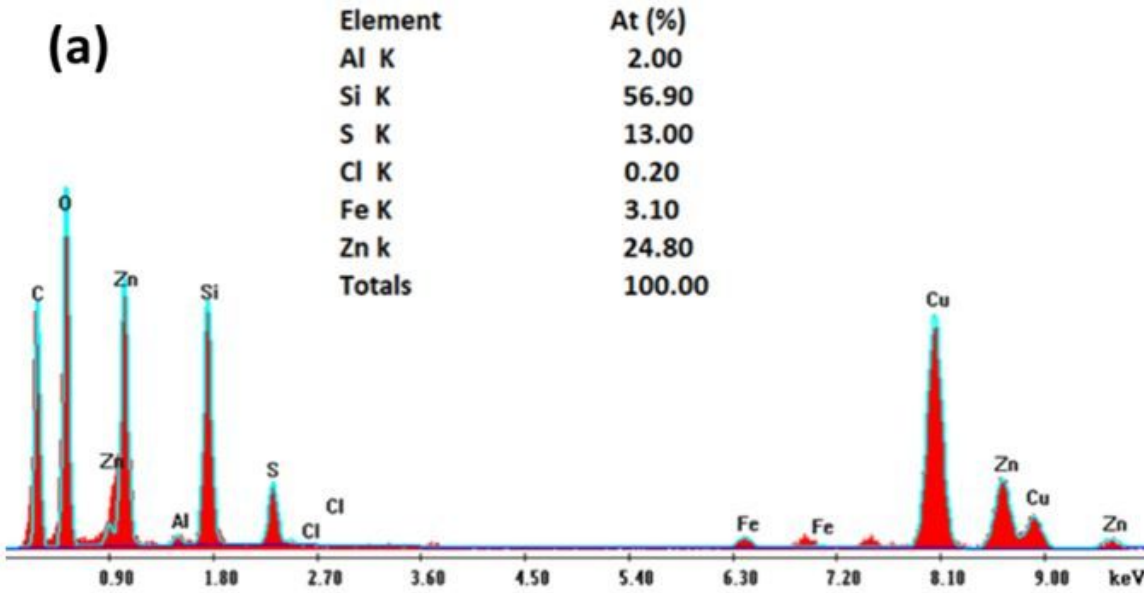
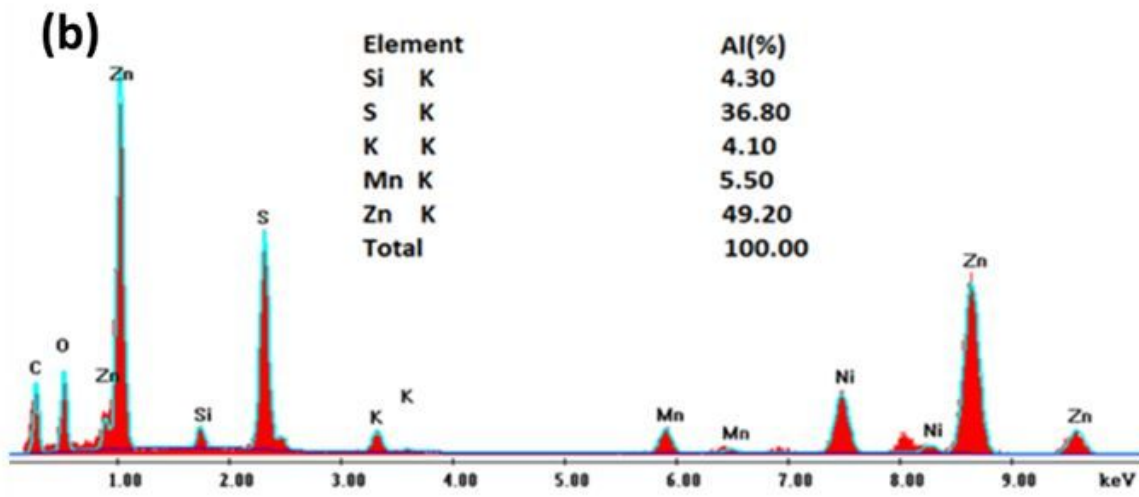


Figure 5

EDX spectrum of (a) undoped and (b) Mn-doped ZnS-TGAnanocrystals.

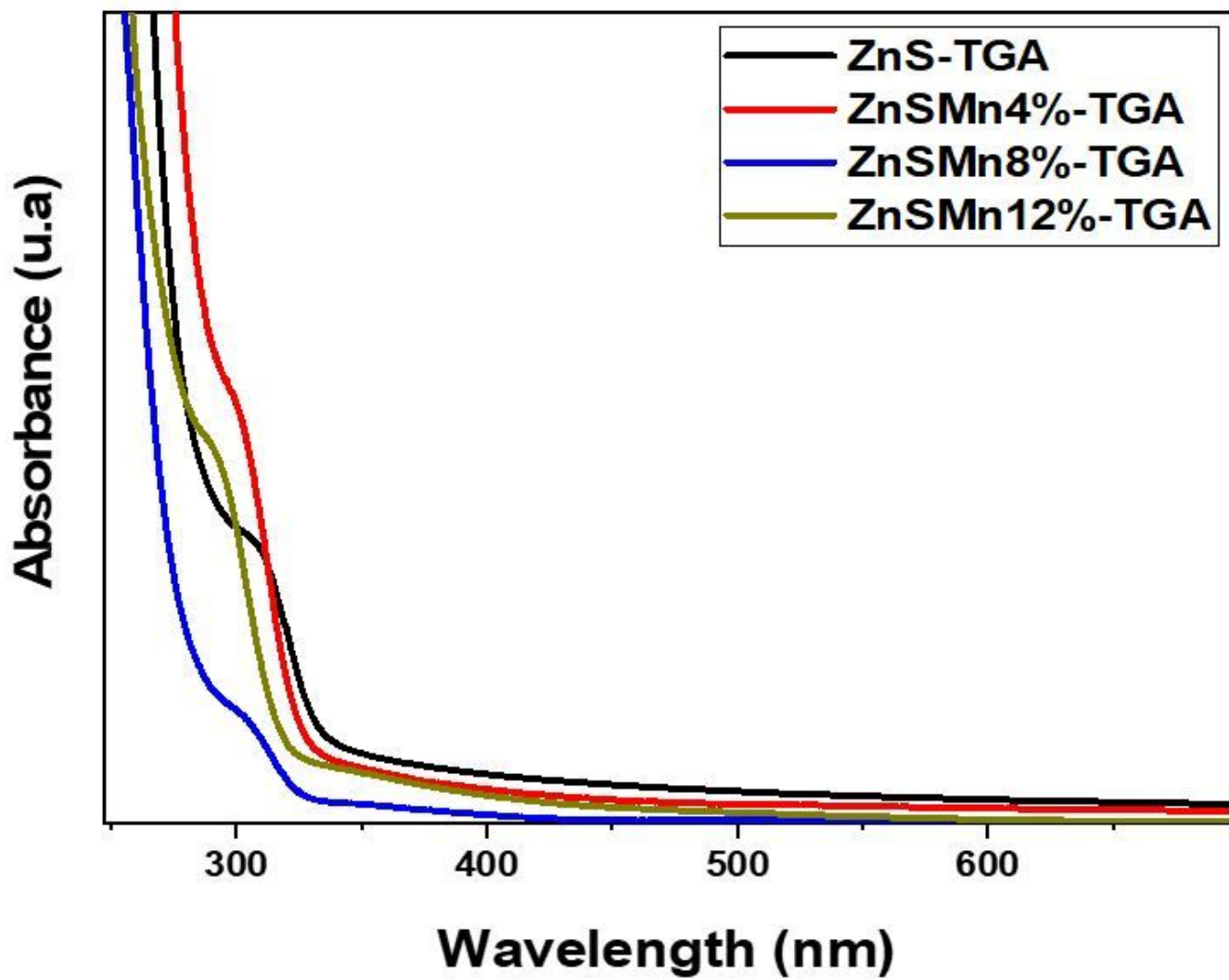


Figure 6

Optical absorption spectra of undoped and Mn-doped ZnS-TGA nanocrystals.

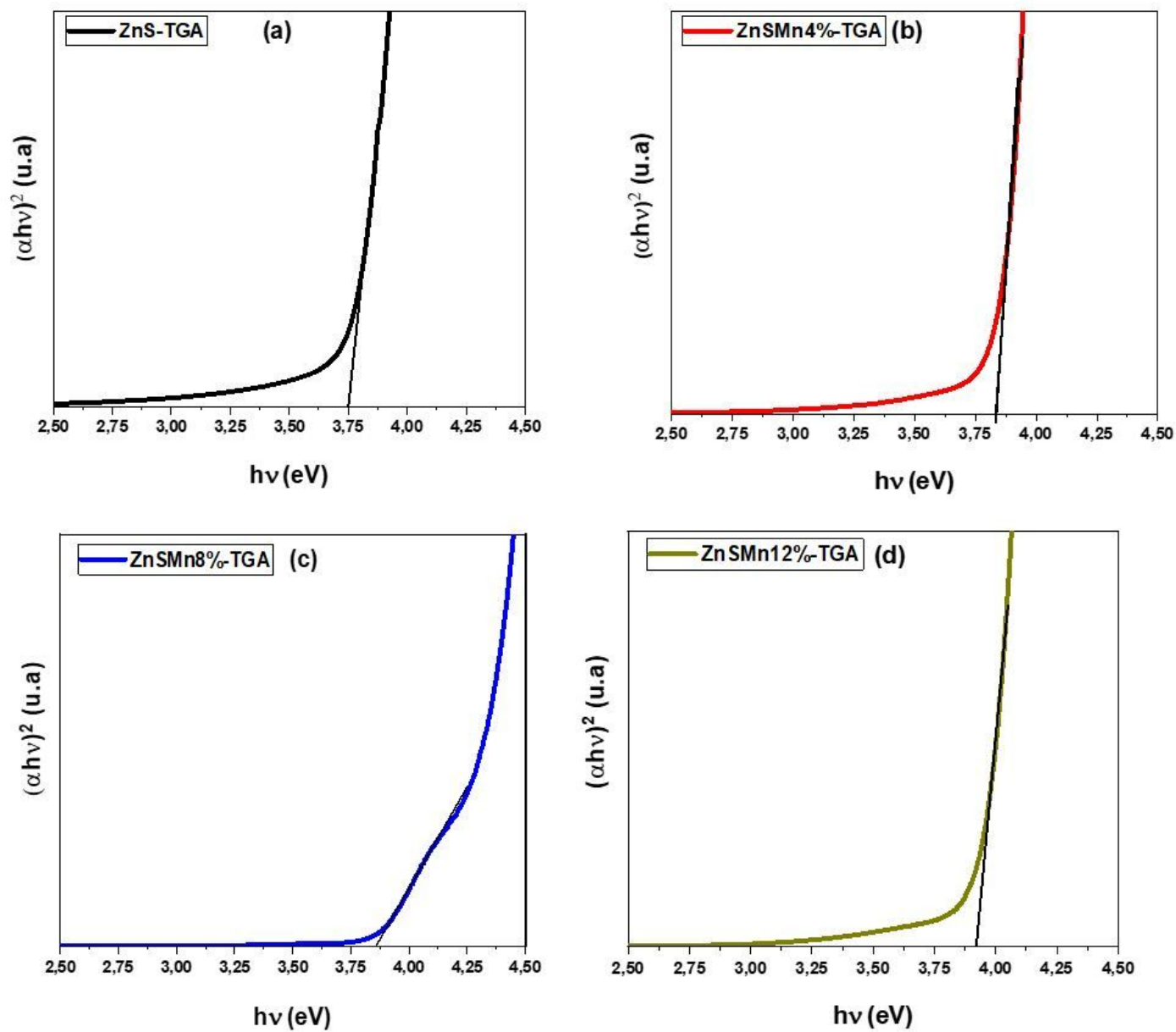


Figure 7

Graphical method for the calculation of the optical gap of (a) undoped and (b-d) Mn-doped ZnS-TGA nanocrystals.

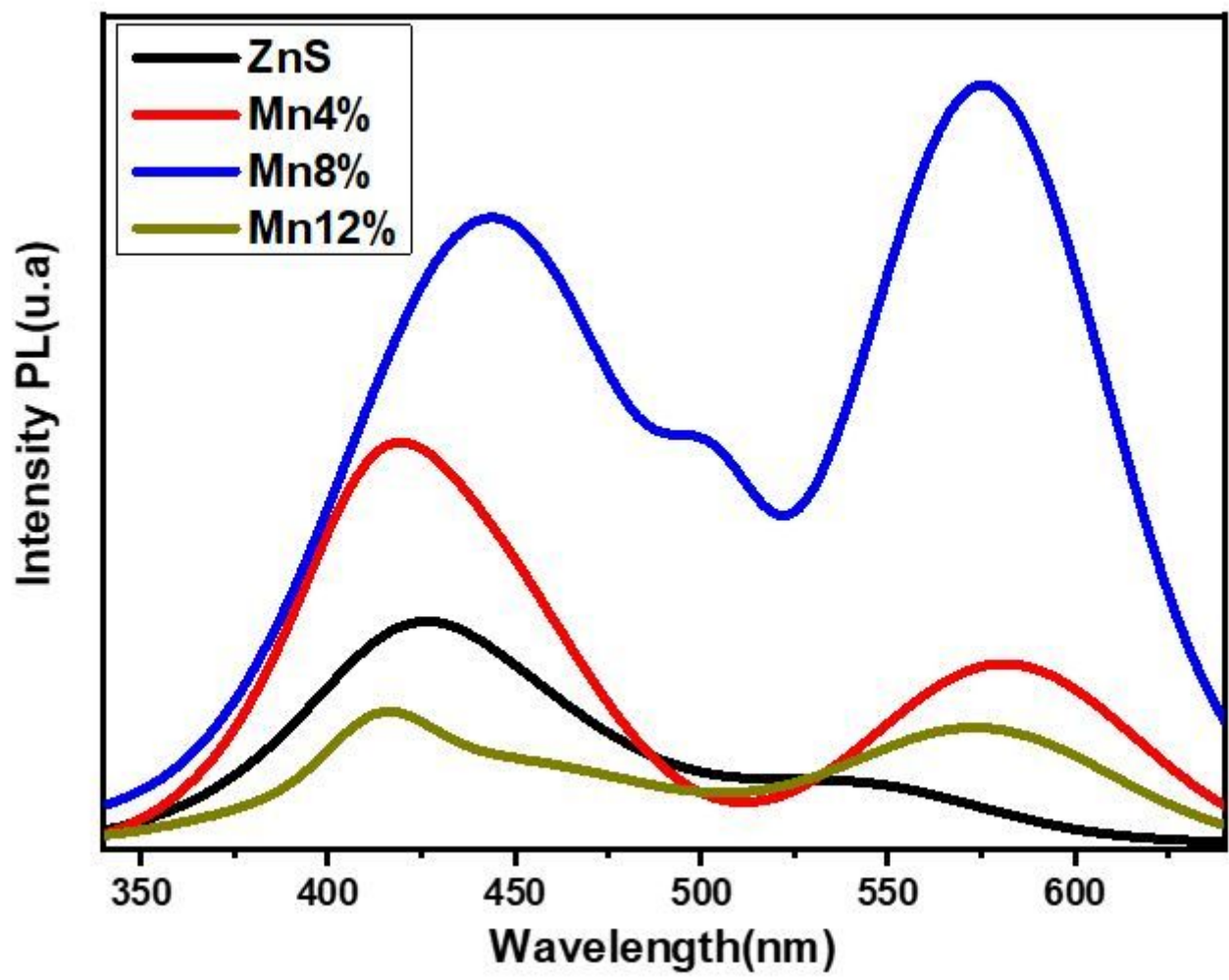


Figure 8

Emission spectra of undoped and Mn-doped ZnS-TGA nanocrystals.

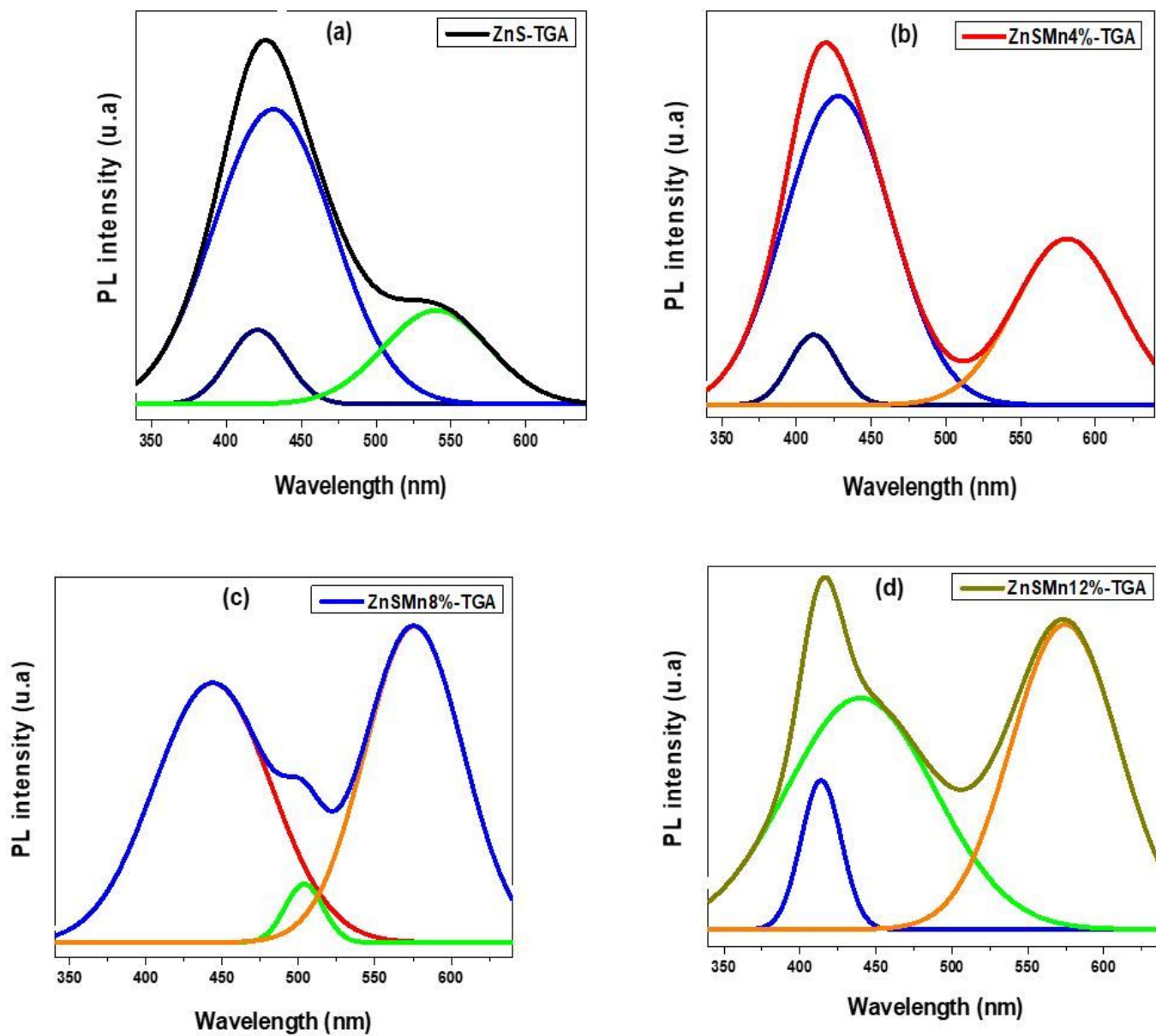


Figure 9

Gaussian adjustment of PL spectra of (a) undoped and (b-d) Mn-doped ZnS-TGA nanocrystals.

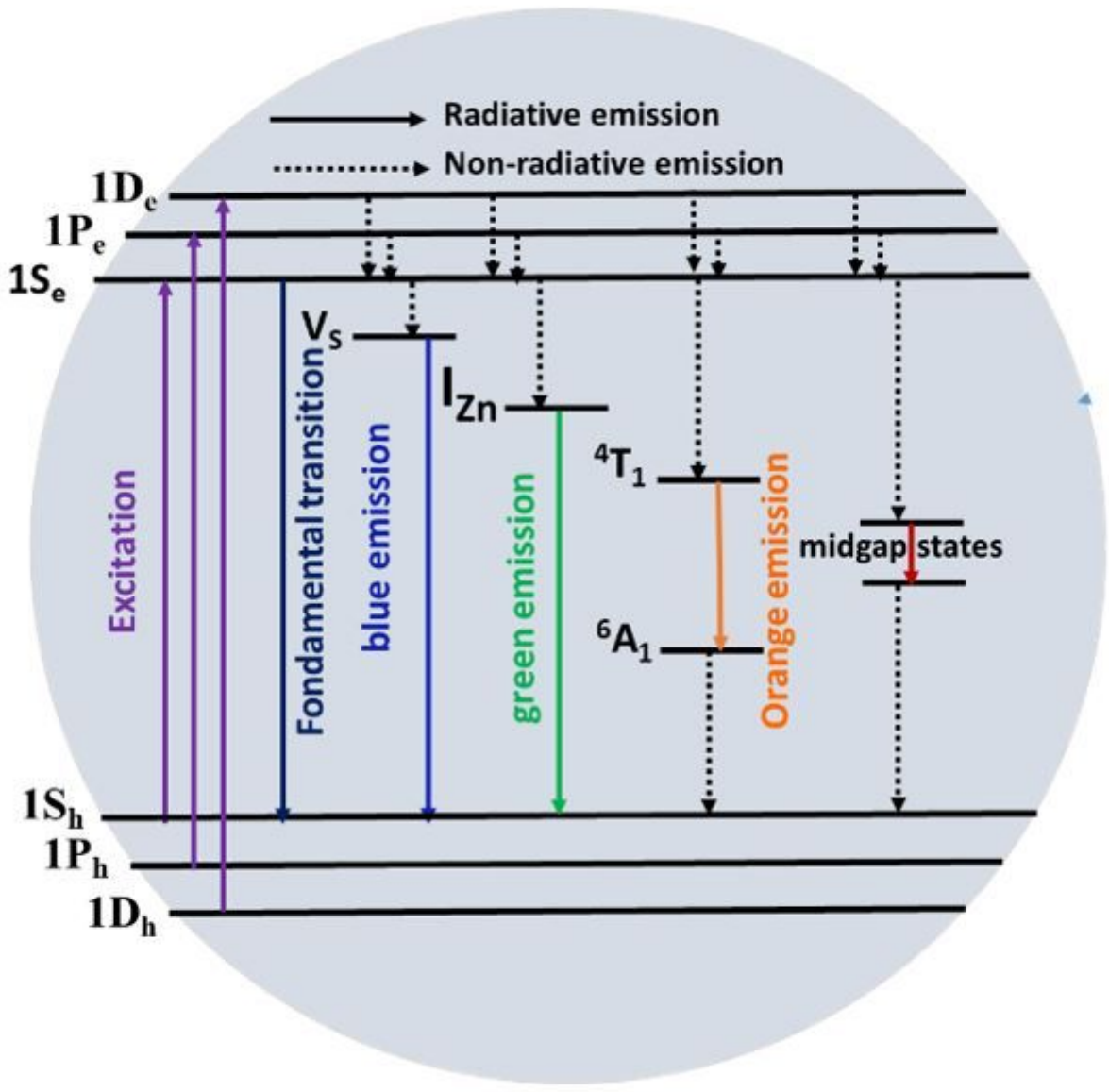


Figure 10

Illustration of emission mechanism of Mn-doped ZnS-TGA nanocrystals.

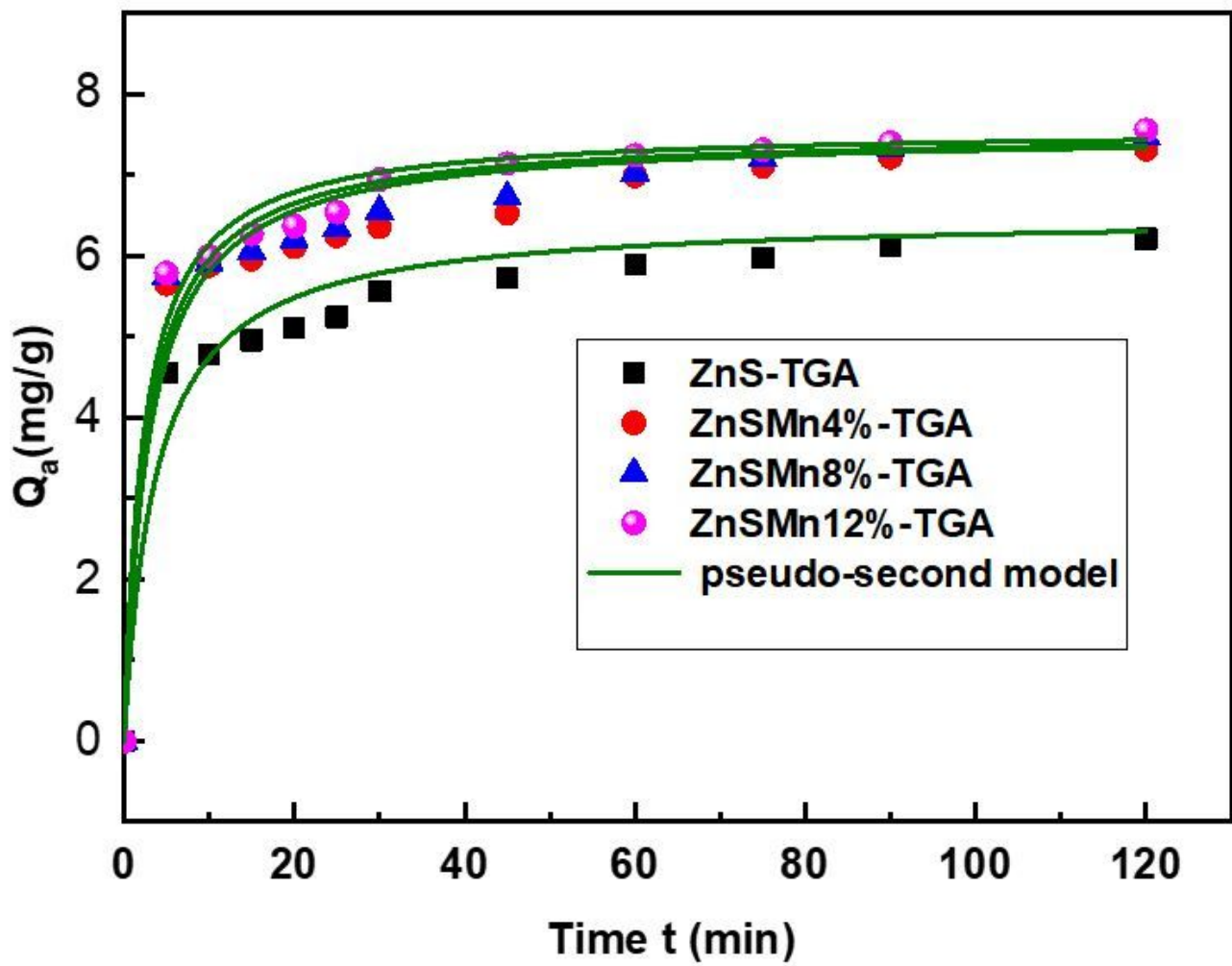


Figure 11

Kinetic adsorption of MO on Mn-doped ZnS-TGA nanocrystals.

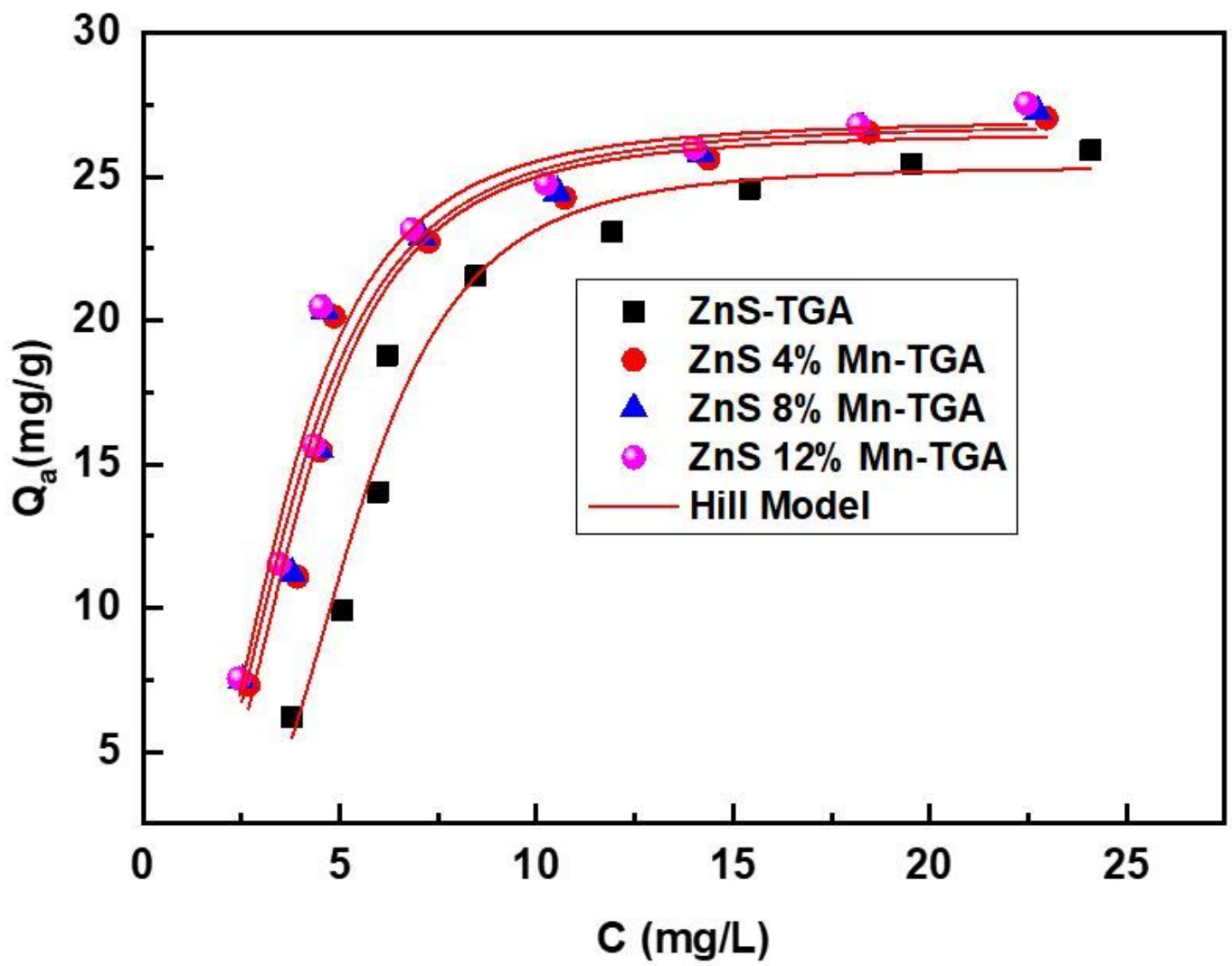


Figure 12

Isotherms of MO adsorption on Mn-doped ZnS-TGA nanocrystals at room temperature

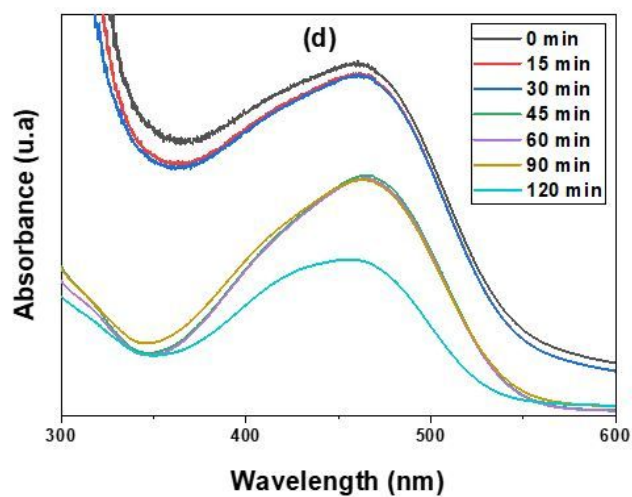
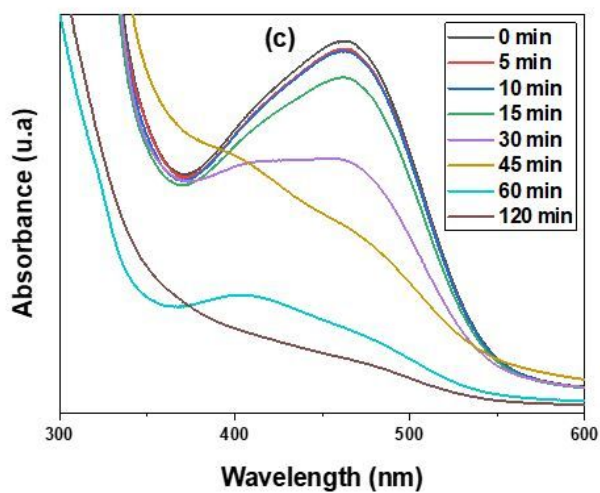
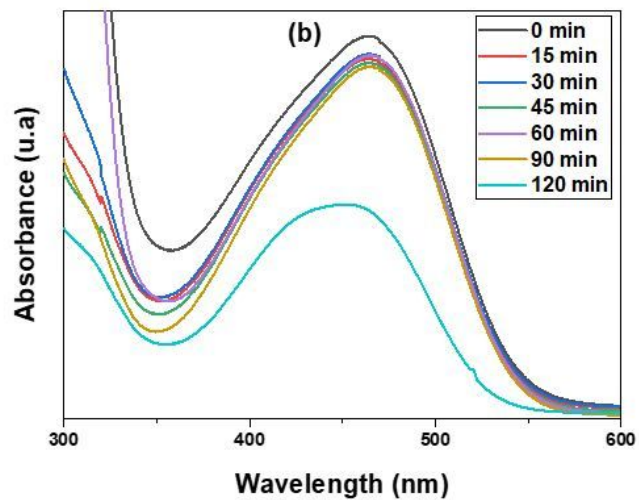
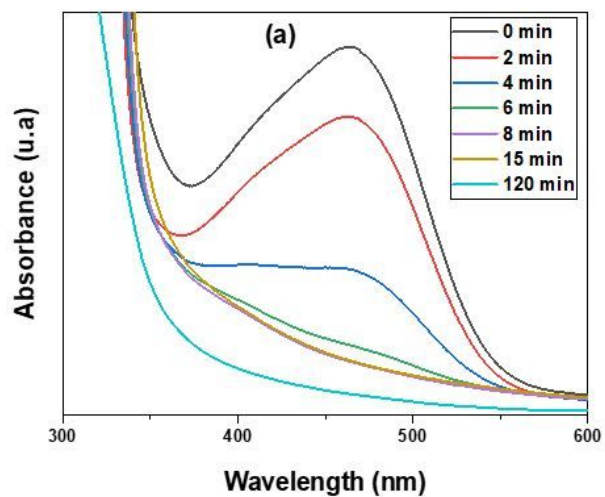


Figure 13

UV-visible absorption spectra of MO solution after photodegradation with (a) undoped and (b-d) Mn-doped ZnS-TGA nanocrystals under UV irradiation.

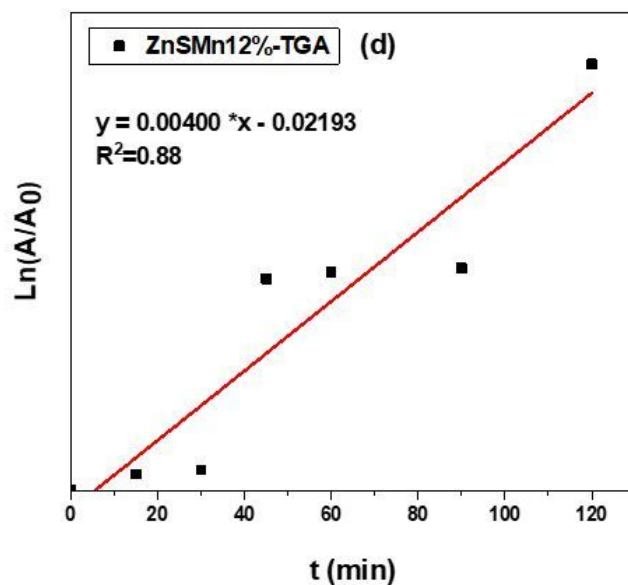
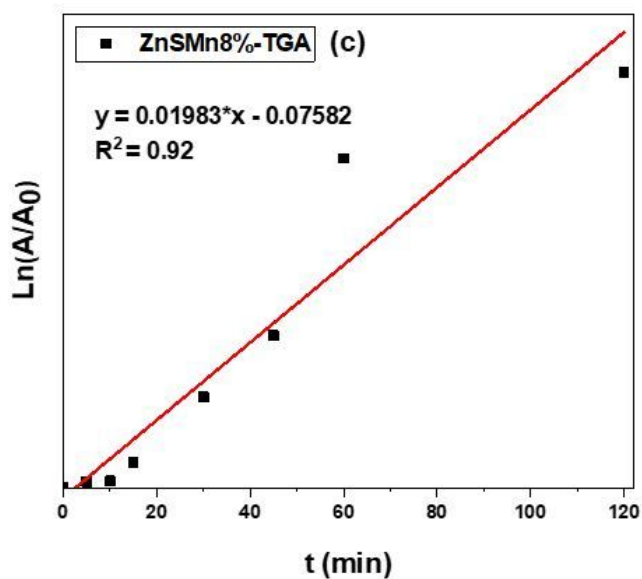
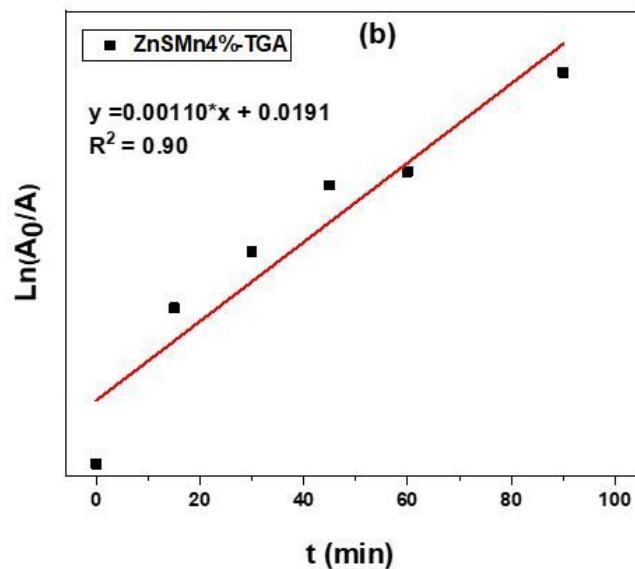
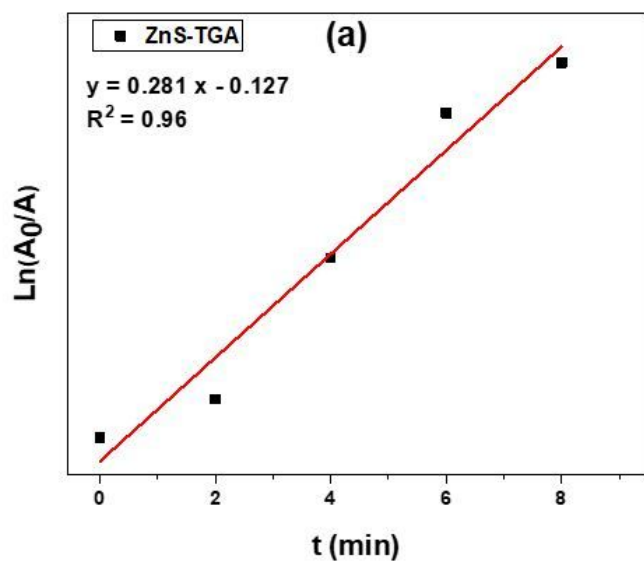


Figure 14

Data correlation for the calculation of degradation rate constants for (a) undoped and (b-d) Mn-doped ZnS-TGA nanocrystals.

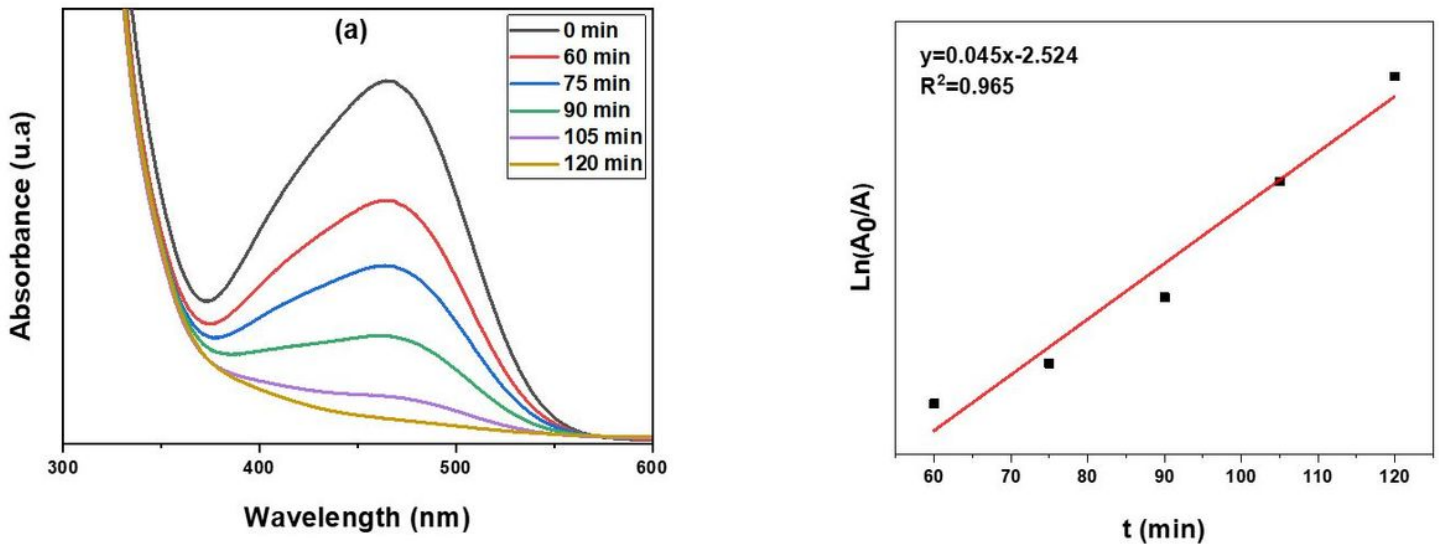


Figure 15

(a) UV-visible absorption spectra of MO solution after photodegradation using ZnS-TGA under sunlight and (b) data correlation for the calculation of degradation rate constant.

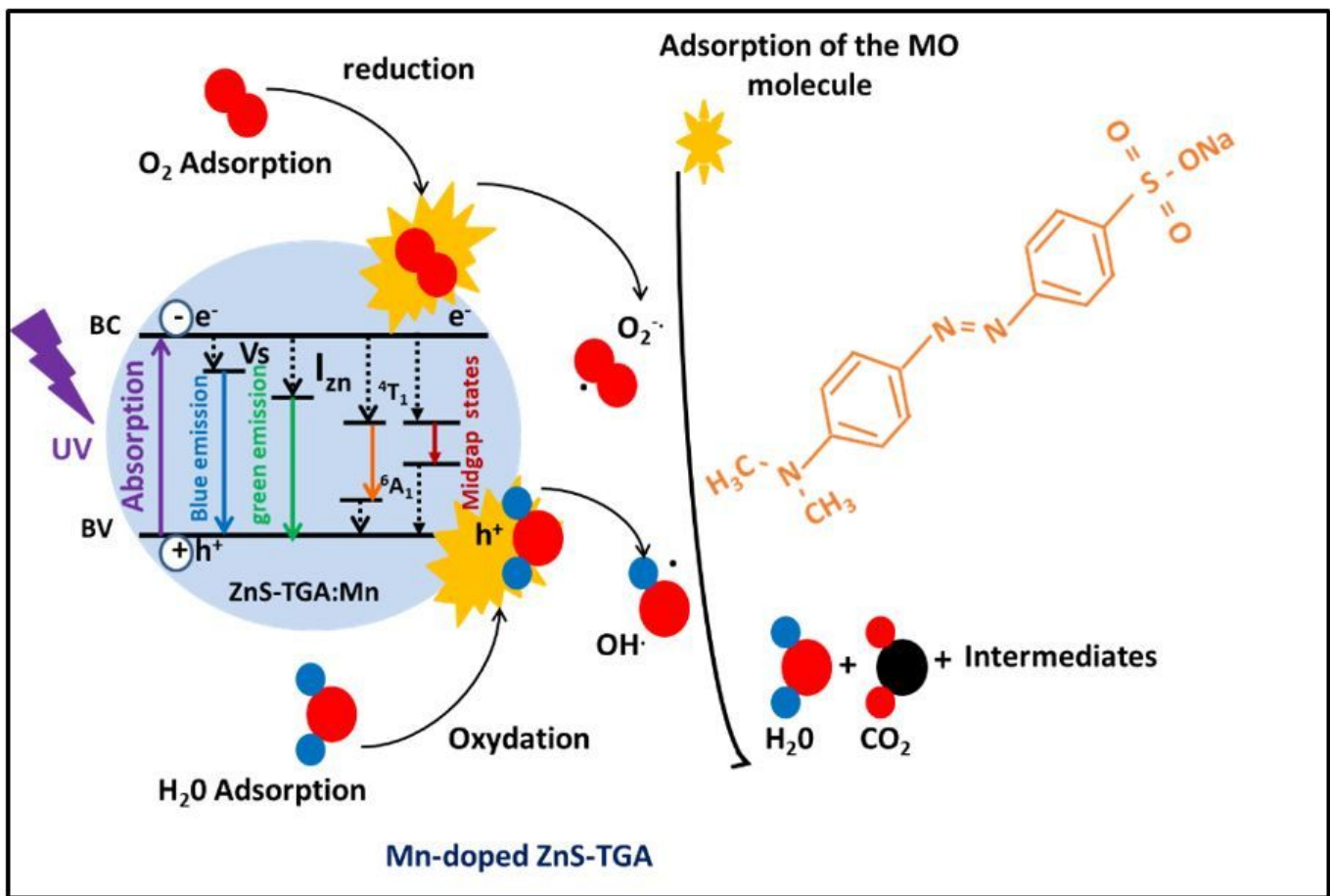


Figure 16

Illustration of the mechanism of degradation of MO using Mn-doped ZnS-TGA nanocrystals.